

## Two paradigms of baroclinic-wave life-cycle behaviour

By C. D. THORNCROFT<sup>1\*</sup>, B. J. HOSKINS<sup>1</sup> and M. E. McINTYRE<sup>2</sup>

<sup>1</sup>*Department of Meteorology, University of Reading*

<sup>2</sup>*Department of Applied Mathematics and Theoretical Physics, University of Cambridge*

(Received 24 October 1991; revised 26 May 1992)

### SUMMARY

Two idealized baroclinic wave-6 life cycles examined here suggest a framework of opposite extremes (a) in which to view the behaviour of real synoptic-scale disturbances in middle latitudes, and (b) in which to interrelate the synoptic and wave-theoretic viewpoints, using the ‘saturation-propagation-saturation’ (SPS) picture of wave-6 life-cycle behaviour. The two life cycles, denoted by LC1 and LC2, are higher-resolution versions of the Simmons–Hoskins ‘basic’ and ‘anomalous’ cases (showing strong and weak late decay of eddy kinetic energy, EKE). They illustrate, in varying degrees, two extreme types of behaviour here designated ‘anticyclonic’ and ‘cyclonic’, and epitomized by strongly contrasting upper-air trough behaviour. ‘Anticyclonic’ behaviour dominates the late stages of LC1 and is characterized by backward-tilted, thinning troughs being advected anticyclonically and equatorward, as in the commoner cases of planetary-scale mid-stratospheric ‘Rossby-wave breaking’. ‘Cyclonic’ behaviour dominates LC2 and is characterized by forward-tilted, broadening troughs wrapping themselves up cyclonically and poleward, producing major cut-off cyclones in high latitudes. These morphologies are visualized by upper-air maps of potential temperature on the nominal tropopause, defined as a constant-potential-vorticity surface. Some atmospheric mid-latitude disturbances examined here, using the same visualization applied to operational analyses, show the same two extreme types of trough behaviour together with intermediate cases.

The SPS picture is re-examined, using Eliassen–Palm and refractive-index cross-sections. It is shown, in particular, by reference to a wave-activity theorem of Haynes, that the late stages of LC2 can be looked upon as a remarkably clear, and morphologically novel, large-amplitude counterpart of the nonlinear reflection scenario of Rossby-wave critical-layer theory. The late stages of LC1, by contrast, look more akin to a nonlinear critical-layer absorption scenario. LC2 exhibits a region of largely undular PV contours adjacent to a region of irreversibly deformed PV contours. In the latter region PV rearrangement, and hence absorption of Rossby-wave activity, has largely ceased. This accounts for the more persistent EKE in the LC2 case.

### 1. INTRODUCTION

The atmosphere exhibits a vast range of cyclone behaviour on various space and time scales. From a potential-vorticity, potential-temperature (PV- $\theta$ ) perspective, this variety is manifested in a wealth of different shapes and distortions of PV contours on isentropic surfaces, and of  $\theta$  contours near the ground. Because of its advective properties the PV- $\theta$  field can usefully be described in terms of these shapes, and dynamical insight into quite complicated nonlinear processes obtained with the help of ‘invertibility’ and related ideas. This approach may be of practical use in forecasting and also in quickly assessing the nature of synoptic events. For a review of PV- $\theta$  concepts and their relevance to cyclone behaviour the reader may consult Hoskins *et al.* 1985 (hereafter HMR); see also, for instance, the pioneering papers by Rossby (1936) and Charney (1948).

Figure 1 shows the general nature of isentropic motion in a mature cyclonic system and its surroundings, looking northwards in the northern hemisphere. This schematic picture draws on the work of several authors (e.g. Danielsen 1964, 1980; Green *et al.* 1966; Carlson 1980; Heckley and Hoskins 1982; Golding 1984). The descending air west of the surface pressure low, on reaching middle levels, splits into two branches A and B turning anticyclonically and cyclonically. Air originating at lower levels in the warm sector equatorward of the surface low rises and splits into two branches C and D. To the extent that condensation occurs in the moist warm-sector branch as it rises, there will be enhanced ascent involving cross-isentropic motion. This pattern of air motion may then result in a cloud pattern with a hammer-head appearance. Note also that since the

\* Corresponding author.

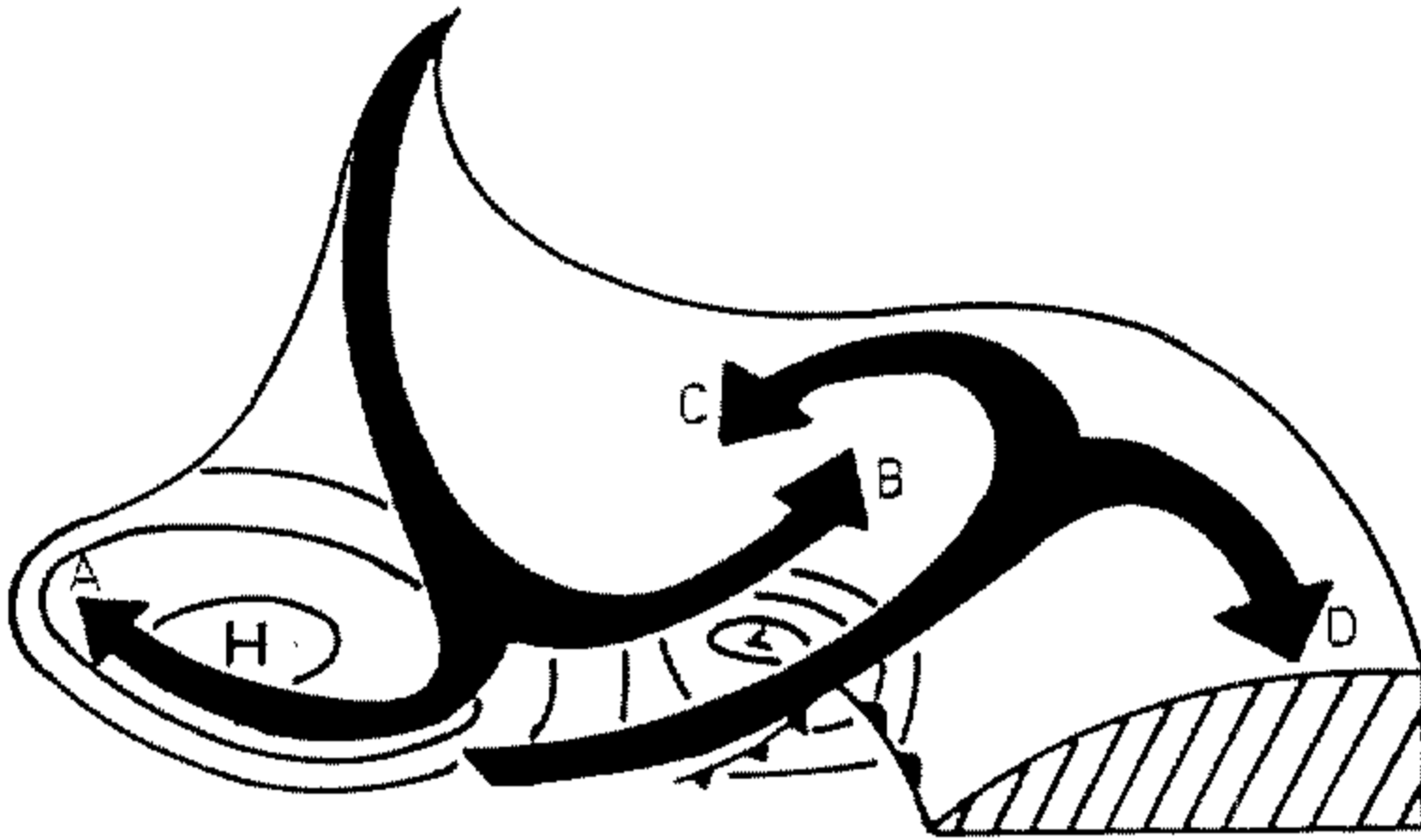


Figure 1. A schematic of isentropic relative flow within a baroclinic wave. Solid arrows represent flow along a sloping isentropic surface. The surface pressure pattern is also indicated (see text for more details).

descending air is certain to be unsaturated, and indeed likely to be very dry, its cyclonic branch B may cut in behind the rising moister air to form a 'dry slot', a feature often observed in strong systems (e.g. Reed and Albright 1986; Young *et al.* 1987).

When considering such systems it is useful to distinguish two extreme types of behaviour. In the first type, most of the flow is in branches A and D, whereas in the second type, most is in B and C. For brevity we refer to these respectively as 'anticyclonic' and 'cyclonic'. Other aspects of the contrast between them will emerge later. Real systems often combine both types of behaviour, as do model baroclinic-wave life-cycle simulations. The purpose of this paper is to show how the distinction is useful for understanding both the real systems and the simulations. In particular, it throws new light on the dynamics underlying the strikingly different energetic behaviours found by Simmons and Hoskins (1980) (hereafter SH) in the two wavenumber-6 cases they denoted as 'basic' and 'anomalous', of which the initial mean flows differ only as regards the horizontal shear.

The present paper is organized into two main parts. Sections 2–6 present analysed synoptic structures and model life-cycle structures, using PV- $\theta$  and other diagnostics. The distinction between the anticyclonic and cyclonic types of behaviour emerges clearly, including a picture of the associated phase tilts and surface frontal structures. In particular, it will be shown that the 'anomalous' wavenumber-6 life cycle is a case of almost purely cyclonic behaviour, while the 'basic' wavenumber-6 life cycle clearly exhibits both types, cyclonic initially and anticyclonic later. It will be suggested that the type of behaviour is strongly influenced by the mean zonal flow and in particular by the strength and sense of its horizontal shear (see especially section 6(c) and Fig. 13). Related research includes that of Hoskins and West (1979) where it was shown that cyclonic horizontal shear included in an initial flow could change the morphology of the baroclinic wave development, and enhance warm frontogenesis. They used uniform-PV flows in a semi-geostrophic framework. Other interesting effects of horizontal shear are discussed by James (1987) in a different context; see also Davies *et al.* (1991), and Hines and Mechoso (1991).

The second part of the present paper (sections 7–9) discusses the dynamical reasons for the two types of behaviour using concepts and diagnostics from wave-mean interaction and related theories. Both the wavenumber-6 life cycles exhibit, more or less clearly, the

'saturation-propagation-saturation' evolution typical of many such life cycles, in which upward Rossby-wave propagation into the mean jet takes over from linear baroclinic instability as the dominant cause of eddy kinetic energy (EKE) growth prior to a final saturation stage. This view of life-cycle dynamics, initiated by Edmon *et al.* (1980) and further developed in several publications (Gill 1982; Hoskins 1983; HMR; Held and Hoskins 1985; Hoskins 1990; Randel and Held 1991) can be combined with insights from nonlinear Rossby-wave critical-layer theory, now a well-understood topic in geophysical fluid dynamics, to illuminate the underlying dynamics in a way that powerfully complements the synoptic viewpoint.

There is at least one very fundamental reason for regarding the anomalous case, in particular, as especially interesting. It will be argued that the behaviour on the poleward side of the jet can be looked upon as a new and morphologically different example of the 'nonlinear reflection' of Rossby-wave activity (more precisely, the non-absorption of such wave activity) predicted by the generalizations of critical-layer theory. In section 8 a recently discovered wave activity conservation relation is used to support this idea, bridging the gap between Rossby-wave critical-layer parameter regimes and the present situation involving far larger amplitudes.

## 2. UPPER-AIR DIAGNOSTIC, AND AN EXAMPLE FROM THE REAL ATMOSPHERE

The upper-air diagnostic to be used in this paper is potential temperature,  $\theta$ , on the  $PV = 2$  surface—more precisely, the surface defined by  $PV = 2PVU$ , where PVU stands for a 'PV unit' of  $10^{-6} \text{ m}^2 \text{ s}^{-1} \text{ K kg}^{-1}$ . This surface is a good approximation to the tropopause for air originating poleward of about  $25^\circ\text{N}$ . A map of  $\theta$  on the  $PV = 2$  surface has the advantage, as compared with a stack of isentropic maps of PV, that it summarizes most of the important upper-level structure in a single picture. It indicates the shape of the tropopause, giving crucial information about the strength and depth of the most important upper-air PV anomalies. One should note also that  $\theta$  is materially conserved on PV surfaces in adiabatic, frictionless conditions. For a fuller discussion see Berrisford (1988), Hoskins and Berrisford (1988) and Hoskins (1990). It should be realized, however, that as it marks the tropopause the  $PV = 2$  surface cannot be used to examine the ascending air originating from the lowest levels of the warm sector.

For the maps presented here the values of  $\theta$  on the  $PV = 2$  surface are found by scanning downwards through the model levels until PV values less than or equal to 2 are encountered. The  $\theta$  value is found by interpolating from the model levels above and below this point. This method is valid only if the PV surface is not multi-valued in the vertical, as might occur if a strong tropopause fold were present. On investigating this problem it was found that, although the tropopause does indeed become distorted in frontal zones, its steepest part tends to remain almost vertical, as far as it could be resolved by the analysis. For the discussion here, PV as well as  $\theta$  can be taken to increase upward, and the present method of interpolation is adequate. But one should be aware that in regions where the maps show a strong  $\theta$  gradient the PV surface may in reality be slightly folded.

Figure 2 illustrates the types of structure seen on the  $PV = 2$  surface in the Atlantic region. Low  $\theta$ -values are generally associated with cyclonic PV and vorticity anomalies, and high  $\theta$ -values with anticyclonic anomalies. This is because of the fact that both  $\theta$  and PV generally increase upward, as just explained. The most prominent features in Fig. 2 are the equatorward low- $\theta$  extrusions, shown hatched. Somewhat loosely, but conveniently, we shall refer to these as 'troughs'. Note especially the structure marked

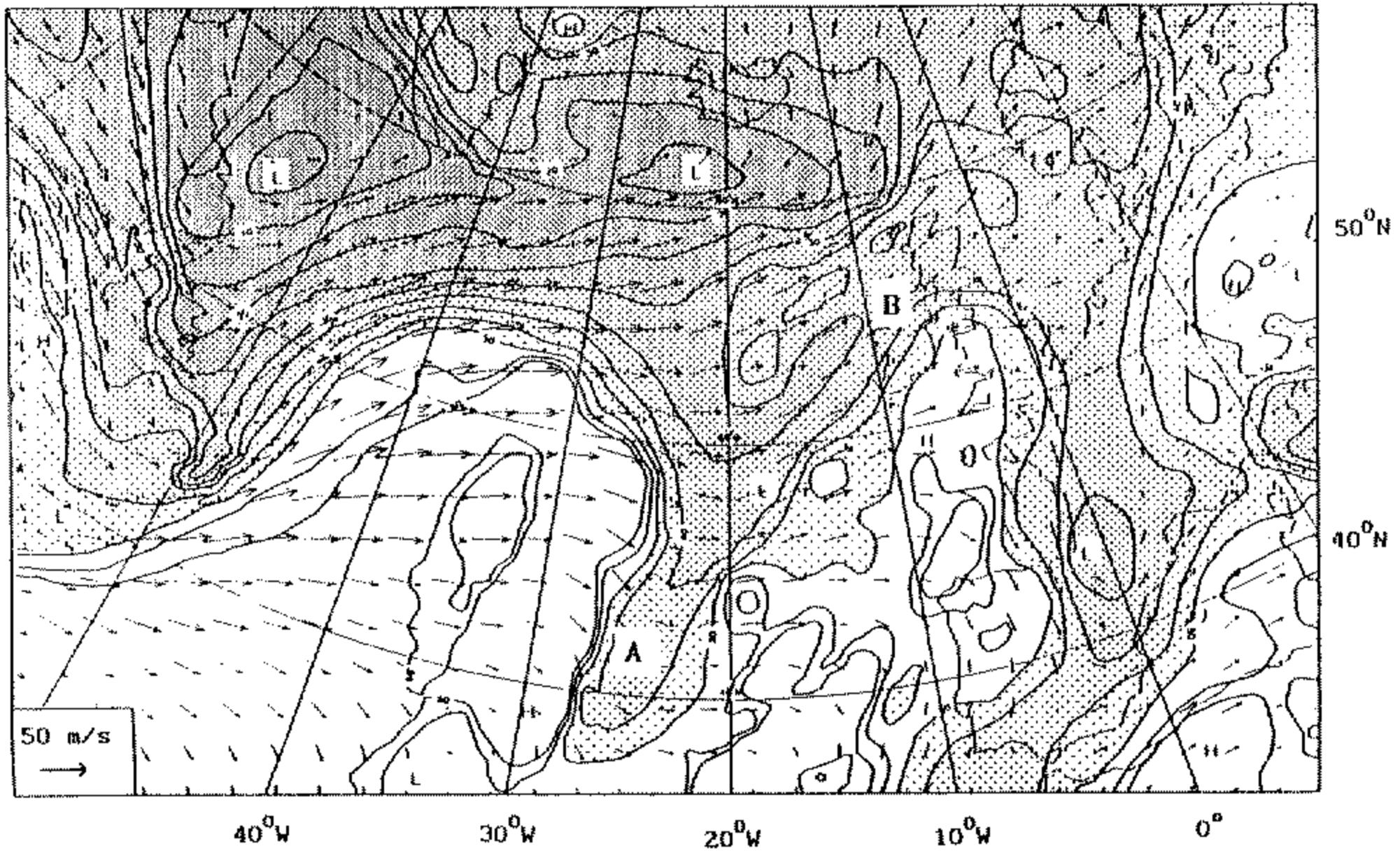


Figure 2. Potential temperature in degrees Celsius on the  $PV = 2$  PVU surface at 12 GMT on 7 January 1990 from the Meteorological Office's fine-mesh analysis. Potential temperatures lower than  $50^{\circ}\text{C}$  are shaded with the lowest values darkest. The contour interval is  $5^{\circ}\text{C}$ . Potential temperatures greater than  $60^{\circ}\text{C}$  are not contoured (see section 6(d)).

AB near  $20^{\circ}\text{W}$ . This suggests that air has turned both anticyclonically to the south and cyclonically to the north, roughly in the manner of branches A and B in Fig. 1. The trough west of this, at  $50^{\circ}\text{W}$ , has a NW–SE tilt while over Europe a NE–SW-tilting trough has produced a cut-off over the Pyrenees. All these trough characteristics will be seen in one or other of the two idealized life cycles presented in this paper.

### 3. THE MODEL

The baroclinic spectral model developed by Hoskins and Simmons (1975) was used in this study, except that the original horizontal resolution, triangular truncation 42 (T42), was improved to T95, giving a resolvable length scale (wavelength/ $2\pi$ ) of about 67 km; 15 sigma levels were used. As in SH, the levels are somewhat concentrated in the region of the tropopause and are given by  $\sigma = 0.967, 0.887, 0.784, 0.674, 0.569, 0.477, 0.400, 0.338, 0.287, 0.241, 0.197, 0.152, 0.106, 0.060$  and  $0.018$  where  $\sigma$  is the pressure divided by the surface pressure. The model is dry and frictionless except for some horizontal internal  $\nabla^6$  hyperdiffusion added to the vorticity, divergence and temperature tendency equations. The diffusion coefficient was chosen to give a decay rate of  $1\text{ h}^{-1}$  for the shortest retained scale,  $n = 95$ . SH used  $\nabla^4$  with  $(6\text{ h})^{-1}$ . The two life cycles presented below were also discussed from a different viewpoint in Thorncroft and Hoskins (1990) (henceforth denoted TH). In that paper the same resolution was used except that the 'basic' life cycle had 30 levels. As mentioned in TH this extra vertical resolution had only a minor effect on the integrations.

### 4. INITIAL CONDITIONS AND EKE EVOLUTION FOR THE TWO LIFE CYCLES

Some of the aspects of the two life cycles have already been discussed by SH, Hoskins (1983), Hoskins (1990) and TH. As in those previous studies, the initial

conditions for the life-cycle experiments consist of a mean zonal flow and a 1 mb surface pressure perturbation of the most unstable mode at zonal wavenumber 6 (hereafter 'modal perturbation'). The initial zonal-mean  $\theta$  is the same function of pressure,  $p$ , and latitude,  $\phi$ , for the two life cycles, and is shown in the top half of Fig. 3, together with the two initial zonal-mean wind distributions. The shading will be explained shortly. Henceforth the first zonal-mean state, shown in Fig. 3(a), will be referred to as Z1 and the second, shown in Fig. 3(b), as Z2. Z1 has a zonal-wind maximum of  $47 \text{ m s}^{-1}$  at about latitude  $45^\circ\text{N}$  on a sloping tropopause, with no wind at the surface. Z2, however, has an added barotropic contribution to the zonal wind that is  $10 \text{ m s}^{-1}$  westerly at  $20^\circ\text{N}$  and  $10 \text{ m s}^{-1}$  easterly at  $50^\circ\text{N}$ . This increases the cyclonic shear of the zonal-mean wind by about  $6 \times 10^{-6} \text{ s}^{-1}$  between these two latitudes. This was originally added to enhance the warm frontogenesis occurring in the growing cyclone, as previously suggested by Hoskins and West (1979). The two life cycles that have Z1 and Z2 in their initial conditions will be referred to as LC1 and LC2, respectively.

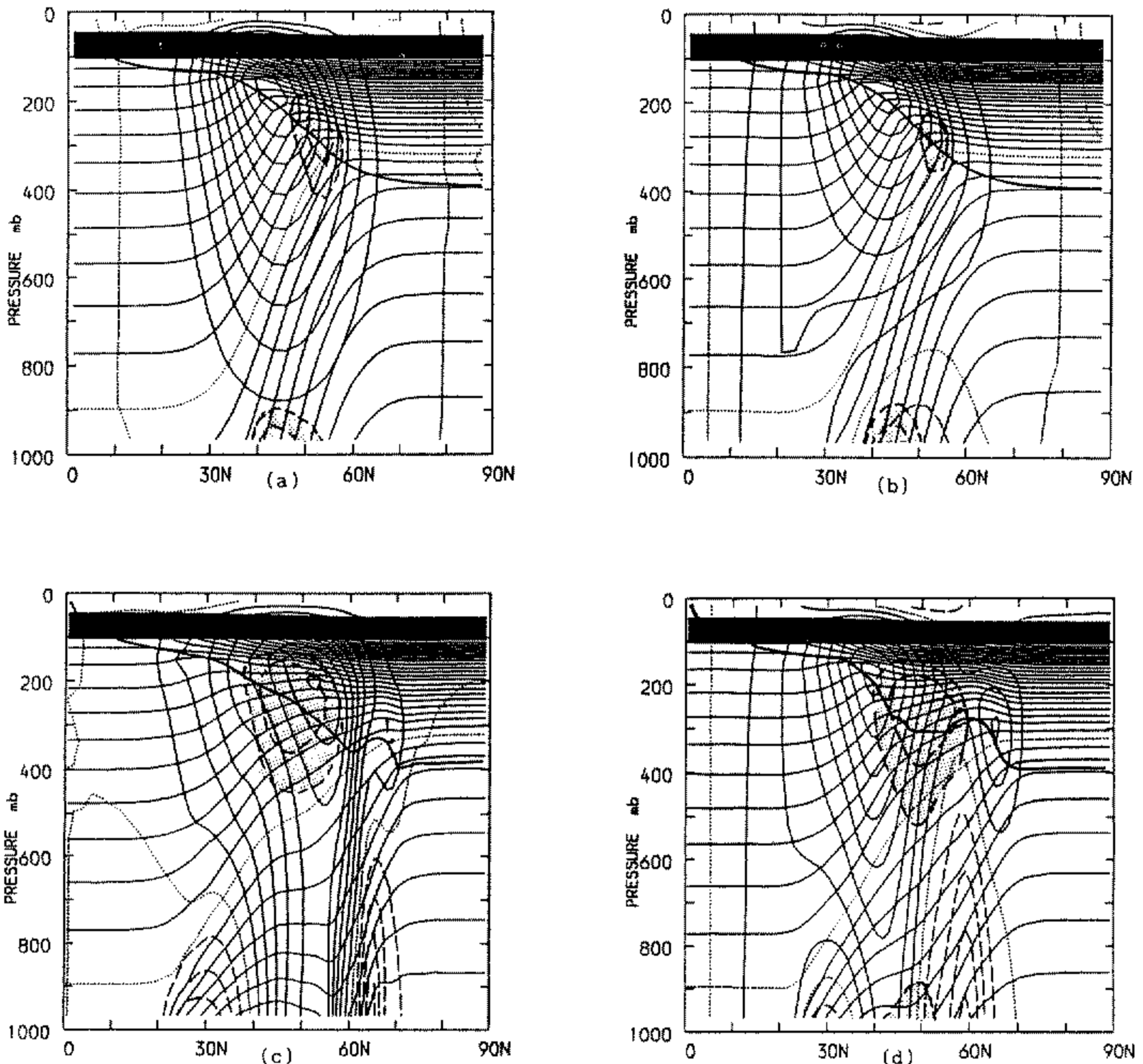


Figure 3. Latitude-height sections showing zonal mean wind with a contour interval of  $5 \text{ m s}^{-1}$  (the dotted line is zero) and potential temperature with a contour interval of  $5 \text{ K}$  (the dotted line is  $300 \text{ K}$ ) for (a) LC1 day 0, (b) LC2 day 0, (c) LC1 day 7 and (d) LC2 day 7. Also marked on these sections is the  $PV = 2 \text{ PVU}$  surface as a solid line sloping upwards towards the tropics. The shaded regions mark the eddy kinetic energy maxima, with dashed contours indicating 0.8 and 0.6 of the maximum in the section.

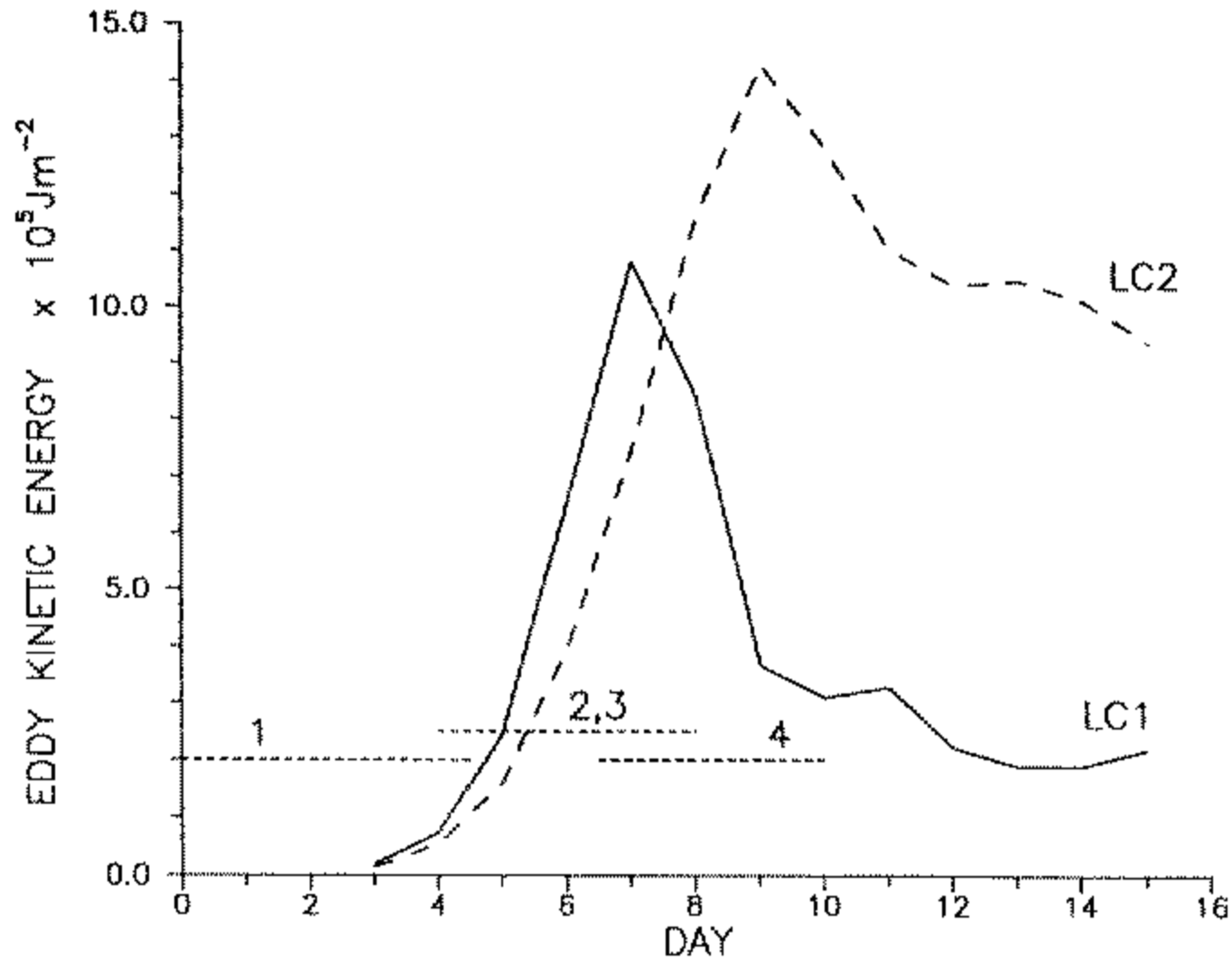


Figure 4. Eddy-kinetic-energy evolution for LC1 (solid) and LC2 (dashed). Also indicated on the graph as horizontal dashed lines are the different overlapping stages of LC1 with numbers corresponding to the discussion in section 7.

Figure 4 shows the evolution of the area-averaged eddy kinetic energy (EKE) for LC1 and LC2. Despite the similar initial growth rates, the maximum amplitude and decay phase are quite different. The respective synoptic evolutions are also very different, as will be seen shortly. Before proceeding, however, we look briefly at the sensitivity to the initial conditions.

Some experiments have been done to examine the effect of changing the amplitude of the initial perturbation and also of using a non-modal perturbation. First, LC1 was repeated with a 10 mb surface-pressure perturbation as initial condition. The life cycle was found to be virtually identical except in the timing, the peak in EKE occurring at about day 3 instead of day 7. In order to see the effect of using a non-modal perturbation, the normal mode from LC2 was scaled, to give a 10 mb surface-pressure perturbation, and added to Z1. Again a very similar life cycle resulted. Similar experiments were done using Z2, with the LC2 normal mode and the LC1 normal mode both scaled to 10 mb. Again, apart from the timing, the main features of these life cycles were similar to those seen in the life cycle initiated with a 1 mb normal mode. We conclude that, even with a 10 mb surface-pressure perturbation, it is largely the initial mean zonal flow, rather than the initial perturbation, that determines what happens in the life cycle.

Referring back to Fig. 4, one sees that the EKE increases initially in both cases. This occurs through baroclinic conversions: ordinary unstable baroclinic growth accounts for the increase up to about day 4 or 5, after which other dynamical processes take over, to be discussed in sections 6–8 and Appendix A. After day 7, the wave in LC1 decays in association with strong barotropic momentum fluxes into the jet. For this life cycle there is a levelling off of the EKE at about day 10 associated with a frontal cyclone event, which was not simulated in the lower resolution integrations of SH (see TH). In contrast, the EKE in LC2 reaches larger values, which also persist for longer. This suggests that the barotropic decay mechanism acting in LC1 is less active in LC2. The momentum fluxes are indeed much weaker in LC2. The more persistent EKE in LC2 is indicative of markedly different nonlinear dynamics resulting from the addition of the barotropic

shear. Note also that the EKE maxima are both greater than in SH, by 20% in the case of LC1 and by 45% in the case of LC2.

The distribution of EKE in the meridional plane gives further information about the differences between LC1 and LC2. The locations of the near-maximum EKE of the two normal modes are indicated by the shading in Fig. 3(a, b). Local maxima exist, one at the surface, and the other at the tropopause in the region of strongest PV gradients (see Figs. 16(c) and 17(c)). In baroclinic instability studies of almost symmetric, uniform-PV jets in  $f$ -plane or flat-earth geometries (e.g. Hoskins and West 1979; Davies *et al.* 1991) the normal modes tend to be centred on the jet maximum, and thus to feel both the cyclonic and anticyclonic shear equally. Since, as demonstrated in different cases by Eady (see Green 1970) and by McIntyre (1970) and Simmons (1974), baroclinic normal modes have a tendency to tilt with the horizontal shear of the basic state, these symmetric flat-earth modes tend to have a crescent shape in the horizontal. In the present case of spherical geometry both the LC1 and LC2 normal modes have most of their upper-level EKE on the cyclonic side of the jet, where the PV gradients are strongest; consistent with this we expect both to be tilted predominantly in the NW–SE direction. This seems to hint that the upper-level disturbances will be influenced more by the mean cyclonic shear than by the mean anticyclonic shear, at least in the early stages of the life cycles.

Figure 3(c, d) shows the mean zonal wind and potential temperature,  $\theta$ , and the EKE-maxima of the disturbances at day 7 for both life cycles. In each case there is a reduction in baroclinicity in middle latitudes, where eddy activity has been strongest. There has also been a pronounced increase in the barotropic component of the mean flow in LC1. This is not so marked in LC2. The mean jet has shifted polewards by about 10 degrees in LC1, but equatorwards by a few degrees in LC2. Note also, for later reference, that the upper EKE maxima have become distinctly stronger than the lower maxima in both life cycles, signalling a departure from normal-mode structure. It can also be seen that in LC1 the upper EKE maximum is now predominantly on the southern, anticyclonic flank of the mean zonal jet, whereas the EKE maximum in LC2 has remained on the northern, cyclonic flank.

Thus there are several indications, from the EKE and zonal-mean diagnostics shown, that the addition of the cyclonic barotropic shear in Z2 results in a very different type of life cycle. In order to see the differences between LC1 and LC2 more clearly, we now examine their synoptic structure and evolution.

## 5. SYNOPTIC EVOLUTION OF THE TWO LIFE CYCLES

### (a) *Life cycle 1 (LC1)*

The low-level temperature evolution between days 4 and 9 for LC1 is shown in Fig. 5. The surface pressure for the same period is shown in Fig. 6. For a detailed description of the surface developments in this life cycle the reader may refer to the discussion by TH. Only a brief commentary on the surface developments is given here.

By day 6 of this life cycle the temperature and surface pressure show many features in common with observed mature systems. Strong temperature gradients in the cold-frontal region trail out from the low-pressure region along the trough line and around the anticyclone, and strong baroclinicity extends around the low-pressure region forming a bent-back baroclinic zone. Associated with this zone are strong surface pressure gradients (Fig. 6). The strong winds associated with this are often observed in deep lows. Moderately warm air has been pinched off by day 6 into the centre of the low. This type of synoptic feature is known as a seclusion, and has occurred in other recent high-

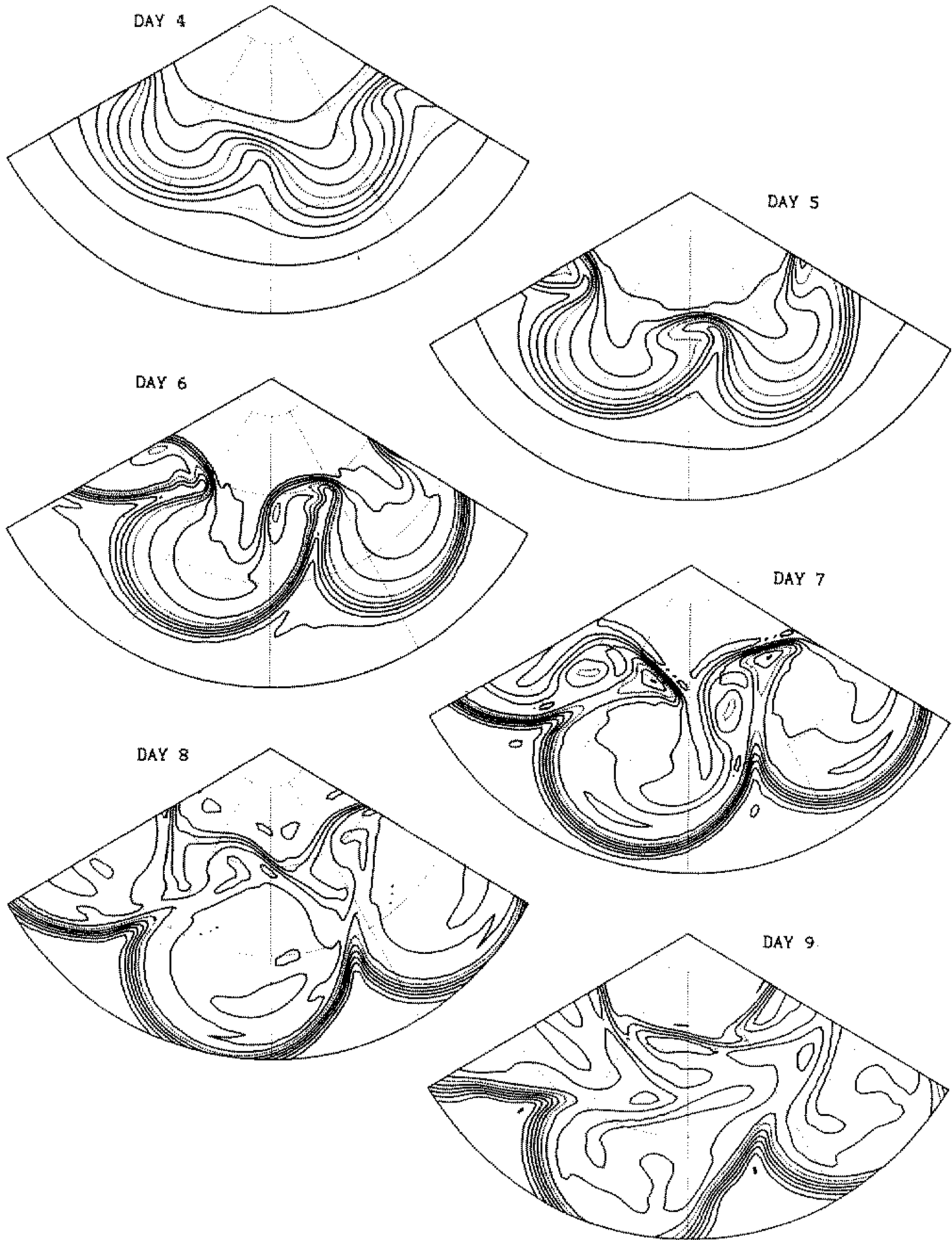


Figure 5. Temperature at  $\sigma = 0.967$  in LC1 between days 4 and 9. Contours are drawn every 4K with the 0°C contour dotted. Sectors are shown for two wavelengths between latitude 20°N and the pole. Lines of constant latitude and longitude are drawn every 20 and 30 degrees, respectively.



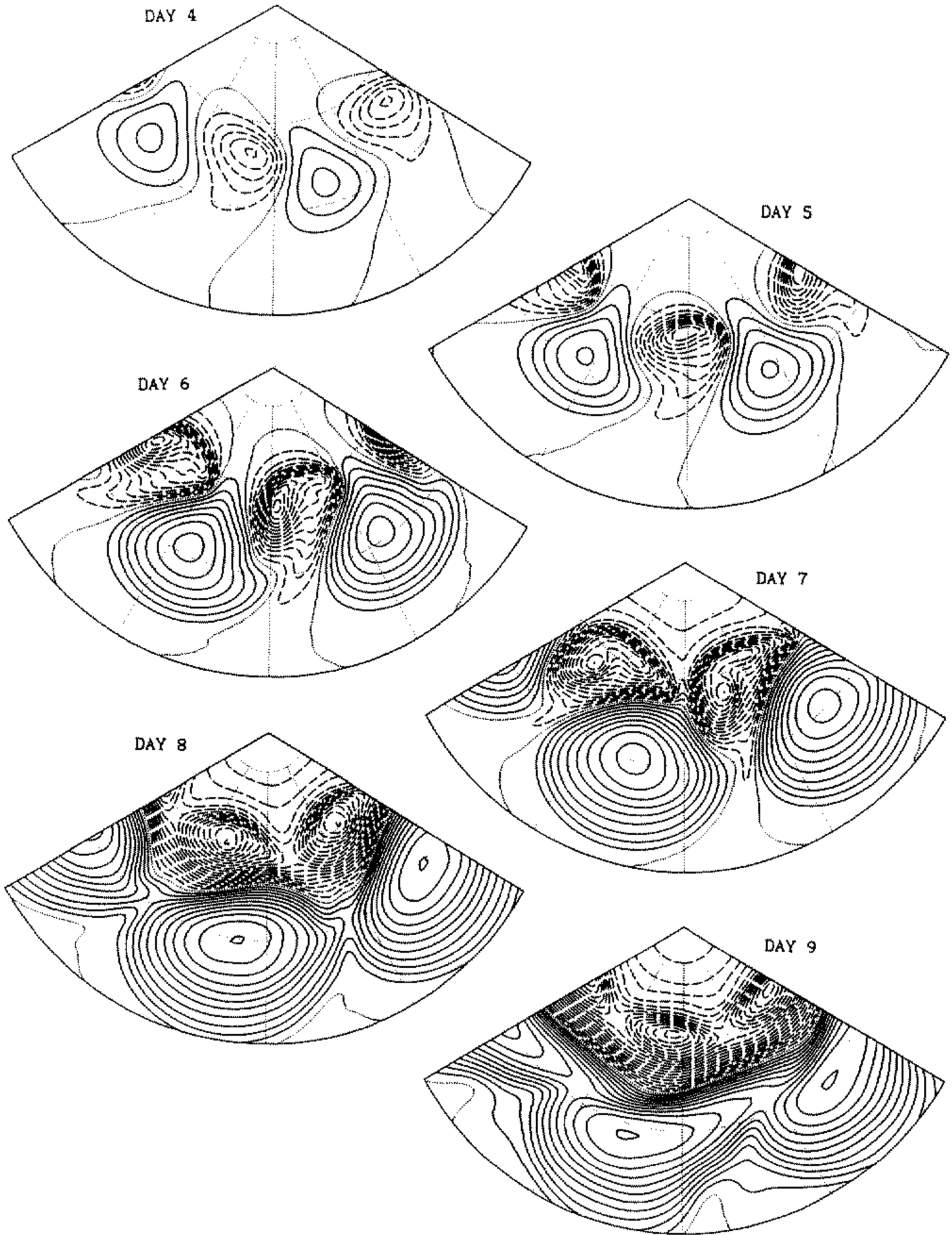


Figure 6. Surface pressure in LC1 between days 4 and 9. Contours are drawn every 4 mb with the 1000 mb contour dotted. Dashed contours indicate surface pressure below 1000 mb. Sectors are shown for two wavelengths between latitude 20°N and the pole. Lines of constant latitude and longitude are drawn every 20 and 30 degrees, respectively.

resolution model integrations (see Shapiro and Keyser 1990). The seclusion process, as seen here, clearly depends on both advection and dissipation. It should also be noted that, by day 6, the cold front has nearly caught up with the trailing baroclinic region of the upstream system. The area of warm-sector air is decreasing, suggestive of a classical 'occlusion' process. However, it should be realized that, in these experiments, the finer-scale features are strongly affected by the model hyperdiffusion. A small-scale wave on the cold front close to the triple point, where the cold front, warm front and bent-back baroclinic zone meet, is also evident at day 6. TH suggested that this may be due to an upstream-development mechanism.

By day 9 the baroclinicity in middle latitudes has been largely destroyed. At the same time the surface pressure has become more zonal, indicating a decaying wave at low levels. There is a second frontal cyclone event becoming apparent on the cold front to the south. Details of its subsequent development are given by TH.

In order to provide a fuller dynamical picture of the synoptic events occurring in the life cycle, the evolution of potential temperature,  $\theta$ , on the  $PV = 2$  surface is now presented. The zonal mean  $PV = 2$  surface is included in Fig. 3 as a solid line sloping upwards towards the tropics. On this surface,  $\theta$  is about 285 K near the pole. In middle latitudes the surface transects several isentropes in the jet region so that, at  $30^\circ\text{N}$ ,  $\theta$  is about 350 K. The evolution of  $\theta$  on the  $PV = 2$  surface is shown between days 4 and 9 (see Fig. 7) and should be compared with the low-level temperature and surface pressure in Figs. 5 and 6.

By day 4, the life cycle is just reaching the end of its exponential growth stage (stage 1 in Fig. 4). We can still see a westward tilt with height going from the position of the warm sector near the ground up to the trough of low  $\theta$ -values on the  $PV = 2$  surface, implying a westward-tilting vorticity maximum, via consideration of the relevant 'PV inversion' problem (see Fig. 18 of HMR). In the horizontal plane, as suggested above, the wave is tilted in the NW–SE direction on the cyclonic side of the mean jet. Between day 4 and 5 the horizontal tilt with the cyclonic shear of the jet becomes more pronounced. By day 5 the  $\theta$  contours on the  $PV = 2$  surface are suggestive of a cyclonic wrapping-up process. Between day 5 and day 6 the low- $\theta$  air that was previously tilted into the jet has turned polewards parallel to the surface cold front, at low as well as high altitudes (Figs. 5 and 7) in a large-scale cyclonic wrapping-up event. Note also that while the low- $\theta$  air is turning cyclonically northwards, in the same manner as branch B in Fig. 1, there is high- $\theta$  air turning cyclonically southwards, in the same manner as branch C. Although this part of the life cycle is predominantly cyclonic in nature, not all of the air moving down the western side of the trough has a cyclonic trajectory. Rather, as in Fig. 1, some air turns anticyclonically and equatorwards (cf. branch A, Fig. 1). It is therefore evident that at about this time there exist both the cyclonic and anticyclonic types of behaviour alluded to in the Introduction.

By day 7 the northward moving low- $\theta$  air corresponding to branch B has been split by the high- $\theta$  southward moving air just behind it, resulting in a low–high–low  $\theta$  pattern within the large-scale trough. Note that the trough now has a marked NE–SW tilt suggesting that it is being affected by the mean anticyclonic shear. Associated with this will be poleward momentum fluxes into the jet and strong barotropic decay of the wave.

Thus, between day 4 and 7 the upper wave has changed from being crescent-shaped with a conspicuous NW–SE horizontal tilt on the poleward side, to being predominantly NE–SW everywhere. This period also corresponds to the migration of the zonal mean EKE from the cyclonic side of the mean zonal jet to the anticyclonic side, as shown by Fig. 3(a, c). The trough in Fig. 7 undergoes marked changes in character after this event. By day 7 there are strong gradients in  $\theta$  on the leading edge of the trough, on the cold-

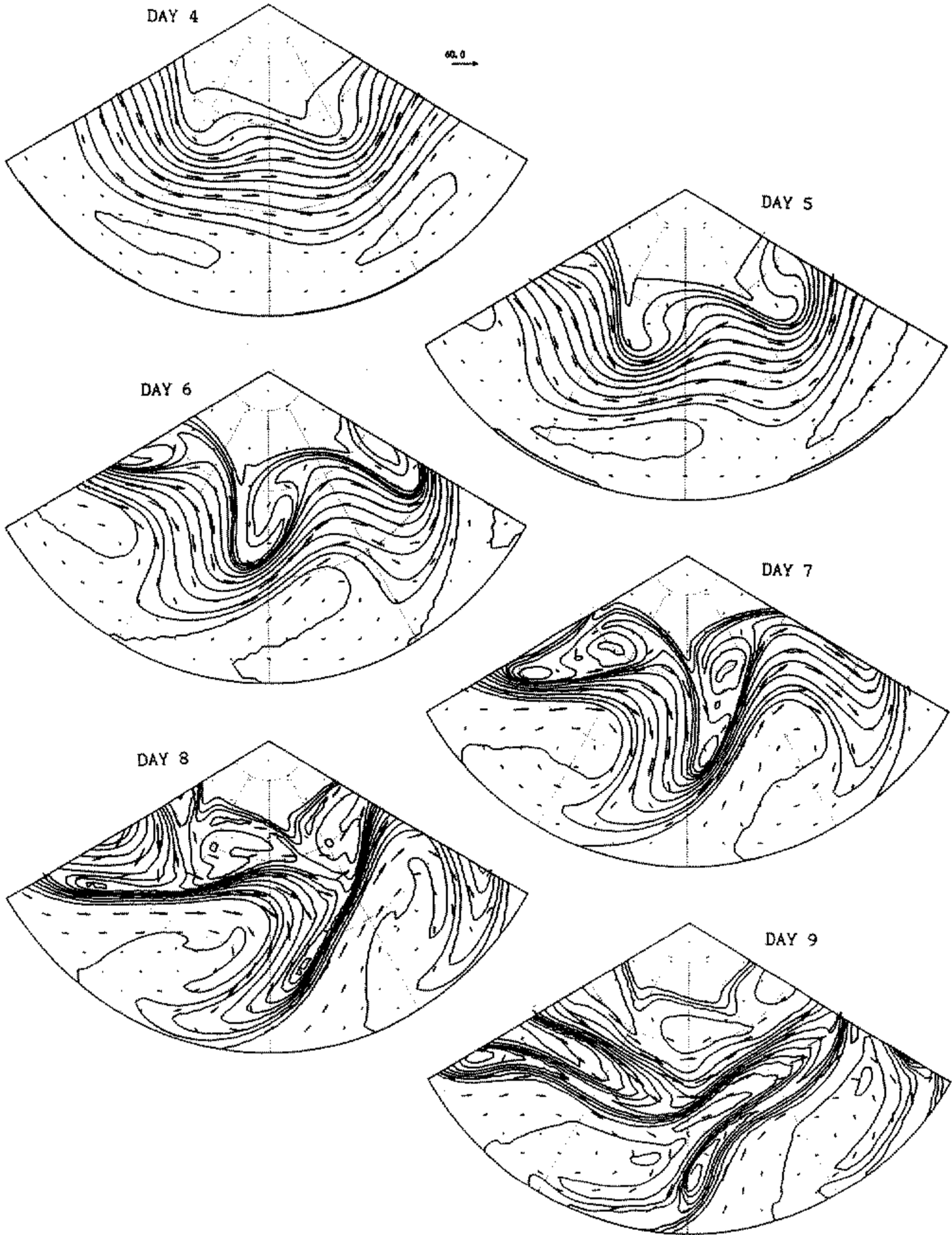


Figure 7. Potential temperature on the  $PV = 2$  PVU surface in LC1 between days 4 and 9. Contours are drawn every 5 K from 290 K to 350 K going equatorward. Wind vectors are included; for days 4 to 7 these have had the phase speed of the normal mode removed to give the relative flow. The arrow scale is as in Fig. 11 (with allowance for the different figure dimensions). Sectors are shown for two wavelengths between latitude  $20^{\circ}\text{N}$  and the pole. Lines of constant latitude and longitude are drawn every 20 and 30 degrees, respectively.

frontal side, and weaker ones at the rear of the trough. Note that the wind vectors are mostly parallel to the  $\theta$ -contours at the leading edge of the trough, whereas there is some cross-contour flow to the rear of the trough. This suggests (see also section 6(c) below) that the trough will thin during the next day as  $\theta$ -contours on the western side of the trough catch up with those on the eastern side. The  $\theta$ -contours are also being advected south-westwards and then westwards around the anticyclone to the south. The whole process is an example of what might be called equatorward 'Rossby-wave breaking', by analogy with the commoner cases of planetary scale Rossby-wave breaking seen in the wintertime middle stratosphere (e.g. Clough *et al.* 1985; McIntyre and Palmer 1984, 1985).

During the next two days (8 and 9) the trough tilts further with the mean anticyclonic shear. As Fig. 4 shows, this is the main barotropic decay period of the life cycle. The trough also becomes thinner as suggested above. By day 9 some low- $\theta$  air from this trough has been cut off to the south. It is this cut-off that subsequently interacts with the surface baroclinicity to initiate a frontal cyclone (see TH for more details). The trough has also continued to wrap up anticyclonically during this equatorward wave-breaking period. This is indicated by the thin streamers of low and high  $\theta$ .

In summary, the life-cycle LC1 exhibits both the cyclonic and anticyclonic types of behaviour described in the Introduction. The wave is initially dominated by cyclonic shear of the mean zonal jet. It tilts in a NW-SE direction and then wraps up cyclonically. Then between days 5 and 7 the wave becomes more affected by the anticyclonic shear to the south of the mean zonal jet. The transition changes the character of the development quite markedly, resulting in an equatorward wave-breaking event characterized by a thinned trough and the formation of a cut-off.

#### (b) *Life cycle 2 (LC2)*

The low-level temperature and surface pressure from days 4 to 9 for LC2 are shown in Figs. 8 and 9, respectively.

The initial temperature wave in this case is more tilted in the NW-SE direction than that in LC1 at the same time, consistent with a stronger mean cyclonic shear; this is still evident at day 4. As suggested by the work of Hoskins and West (1979) the strongest temperature gradients are now in the warm-frontal zone. The surface pressure also tilts more strongly NW-SE. By day 6 the warm-frontal temperature gradients have moved westwards around the surface cyclone as before, and, again, warm air has been pinched off into the centre. The warm front remains more marked than the cold front. There is a small ripple on the cold front close to the triple point, as in LC1. The surface cyclone in this case appears to be broader in the zonal direction than in LC1, but more confined in the meridional direction.

By day 7 the magnitudes of the cold-frontal temperature gradients almost match those of the warm front. A large seclusion of warm air is now located in the core of the surface cyclone, which is now nearly circular. By this time in LC1, the surface anticyclones are more prominent than the cyclones (see Fig. 6). In LC2 (Fig. 9), however, it appears that there is less meridional displacement of the systems, and that the cyclones are becoming more prominent than the anticyclones as they deepen and expand.

During the next two days the surface cyclones continue to expand, with the strongest pressure gradients to their northern and western sides. There is still warm secluded air in the centre of each cyclone, and the frontal regions are still connected to the northern part of the wave. This stage of development of LC2 is very different from the corresponding stage in LC1, which is more nearly zonal by day 9, the whole disturbance having undergone strong barotropic decay.

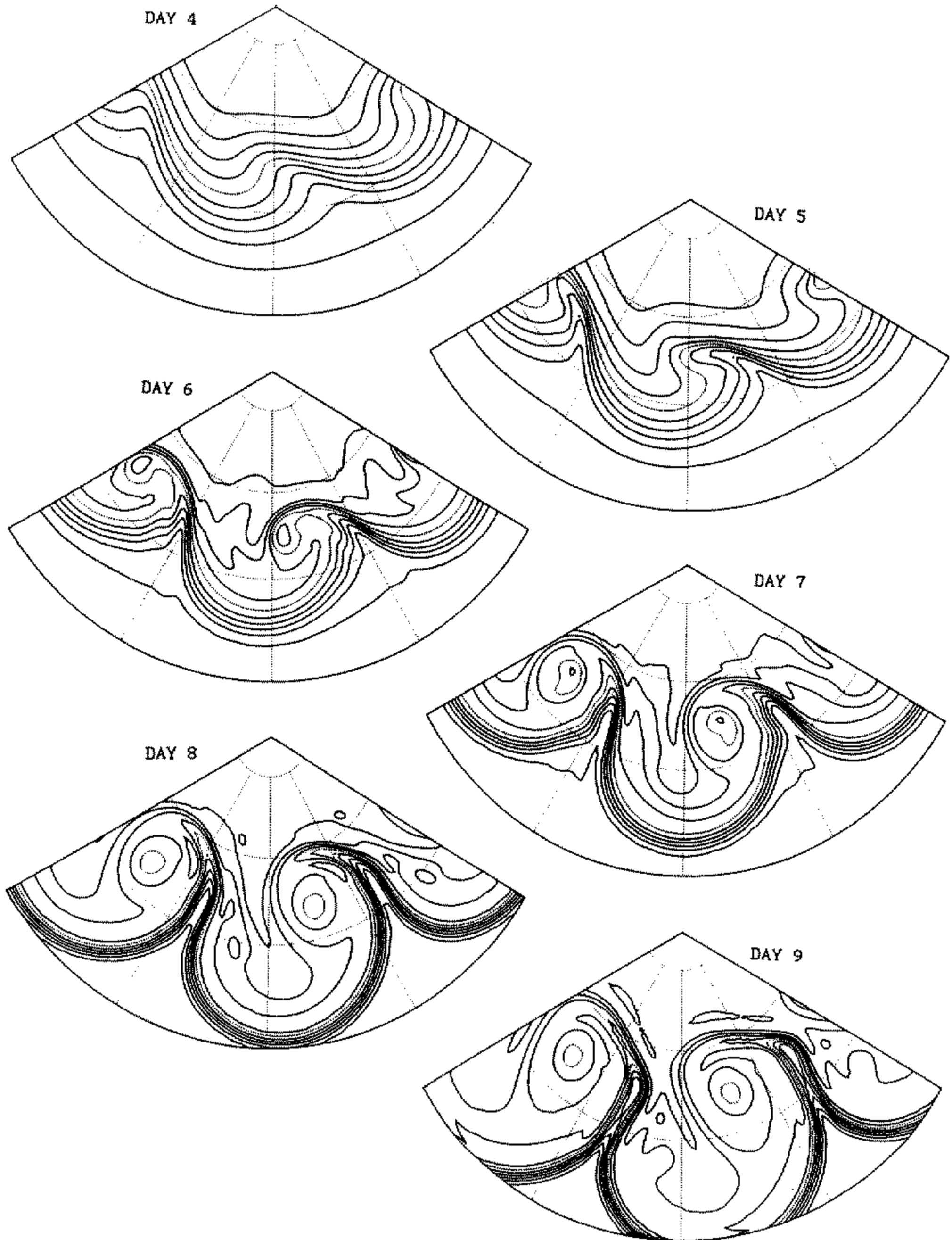


Figure 8. Temperature at  $\sigma = 0.967$  in LC2 between days 4 and 9. Contours are drawn every 4K with the 0°C contour dotted. Sectors are shown for two wavelengths between latitude 20°N and the pole. Lines of constant latitude and longitude are drawn every 20 and 30 degrees, respectively.

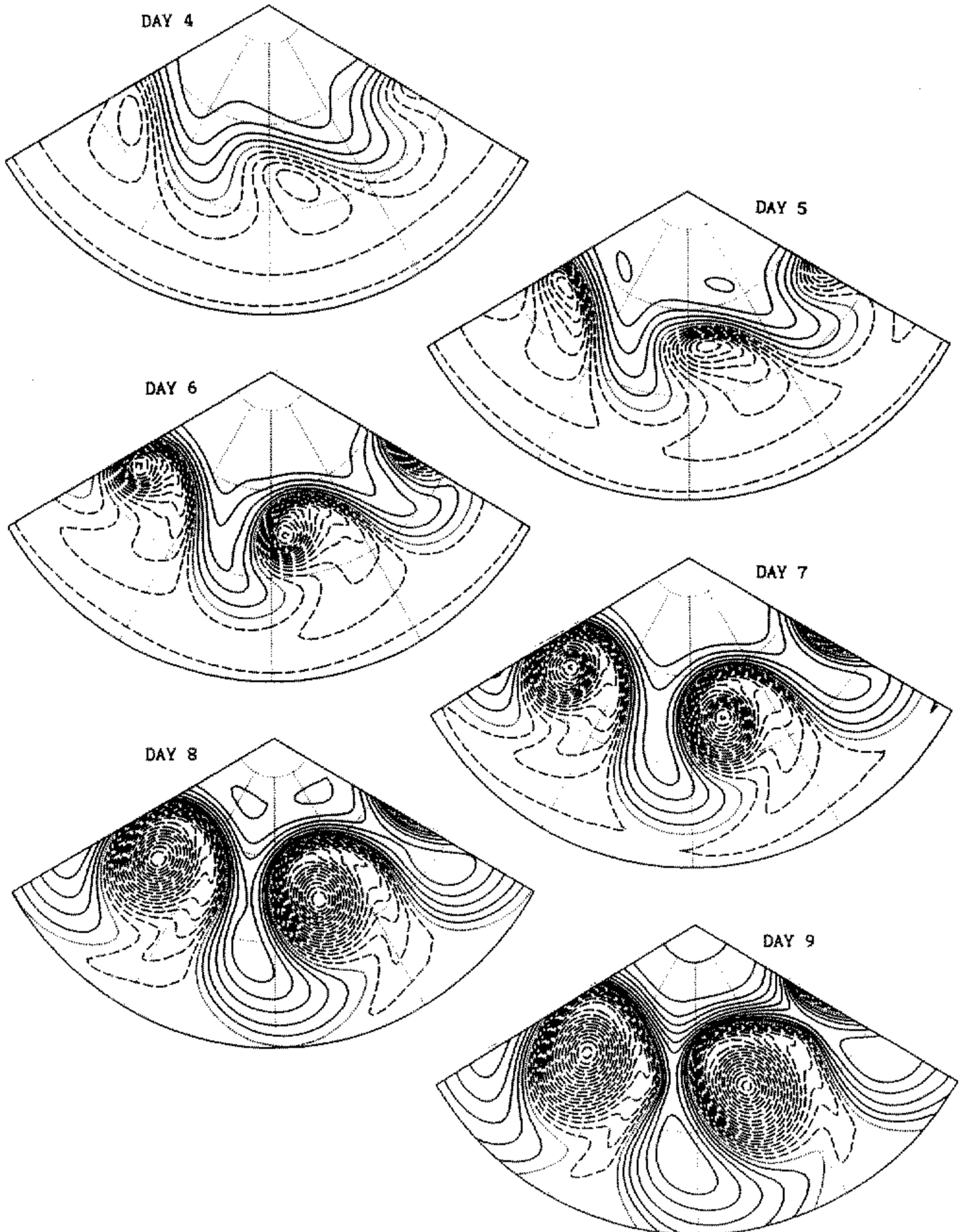


Figure 9. Surface pressure in LC2 between days 4 and 9. Contours are drawn every 4 mb with the 1000 mb contour dotted. Dashed contours indicate surface pressure below 1000 mb. Sectors are shown for two wavelengths between latitude  $20^{\circ}\text{N}$  and the pole. Lines of constant latitude and longitude are drawn every 20 and 30 degrees, respectively.

Figure 10 shows the upper-air evolution for LC2, again using potential temperature,  $\theta$ , on the  $PV = 2$  surface, between days 4 and 9. Initially the distribution of  $\theta$  is fairly similar to that in LC1, although the wave is more tilted on the cyclonic side of the jet. As in LC1 the cold air turns polewards and cyclonically between days 5 and 6, but in a more nearly circular pattern. It is of interest to note that the trough, as with the temperature wave, is broader in the zonal direction but meridionally more confined than in LC1. There is, however, a little anticyclonic turning in the subtropics, though clearly this is much weaker than in LC1.

Whereas by day 7 the trough in LC1 was almost totally dominated by the anticyclonic shear south of the mean zonal jet, the trough in LC2 continues to wrap up air cyclonically. Strong  $\theta$ -gradients exist around the edge of the cyclonic vortex. In contrast with LC1, there are signs of only weak equatorward breaking to the south.

The large-scale cyclonic wrap-up continues up to day 9. Note that, during this time,  $\theta$  inside the vortex becomes uniform, and sharp gradients are generated at the edge. The homogenization of a weakly diffusing, but otherwise materially conserved, quantity, as seen here, has been studied by many authors (e.g. Thomson 1887; Rhines and Young 1983). The essential phenomenon is the shearing together of opposite-signed anomalies into close juxtaposition, promoting their mutual annihilation by any kind of weak diffusive or hyperdiffusive transport such as that in our model.

Also shown here, in Fig. 11, for later use, is the distribution of  $\theta$  on  $PV = 2$  for LC2 at days 11 and 15. As can be seen, the large-scale vortices resulting from cyclonic wrap-up, and their homogenized constant- $\theta$  cores, are remarkably persistent.

In summary, the nonlinear development in LC2 is very different from that in LC1. The wave is relatively little affected by the anticyclonic shear on the equatorward side of the mean jet, and does not reach such low latitudes, decay barotropically, or break equatorwards to nearly the same extent as in LC1. Instead, the cyclonic wrap-up on the poleward side, which also occurred early in LC1, continues and expands to a much larger scale, while  $PV$ - $\theta$  contours near the jet core remain largely undular.

## 6. DISCUSSION

### (a) *Anticyclonic-type and cyclonic-type behaviour*

Viewing the two life cycles in terms of the ideas summarized in Fig. 1, we see that LC1 starts with a cyclonic type of behaviour and changes to a predominantly anticyclonic type, with a transition period at around day 6 when both cyclonic and anticyclonic behaviour are conspicuous. LC2, however, remains predominantly cyclonic. In association with these differences there are two quite different nonlinear developments. LC1 produces a thinned upper-level trough and a small-scale cut-off cyclone as the trough wraps up anticyclonically in an equatorward wave-breaking event. LC2 has a more meridionally confined system exhibiting poleward wrap-up into a large-scale cyclonic vortex, which decays only very slowly.

The migration of each EKE maximum relative to the mean zonal jet (Fig. 3) appears to be linked to the type of behaviour, cyclonic versus anticyclonic, seen in the synoptic evolution presented above. At upper levels both waves have their largest EKE values initially on the cyclonic side of the jet, where the strongest upper-level  $PV$  gradients occur. Unlike the wave in LC2, however, the wave in LC1 has an EKE maximum that migrates equatorward relative to the mean jet core, suggesting that the wave then comes more under the influence of the anticyclonic mean shear. In some sense, the jet appears

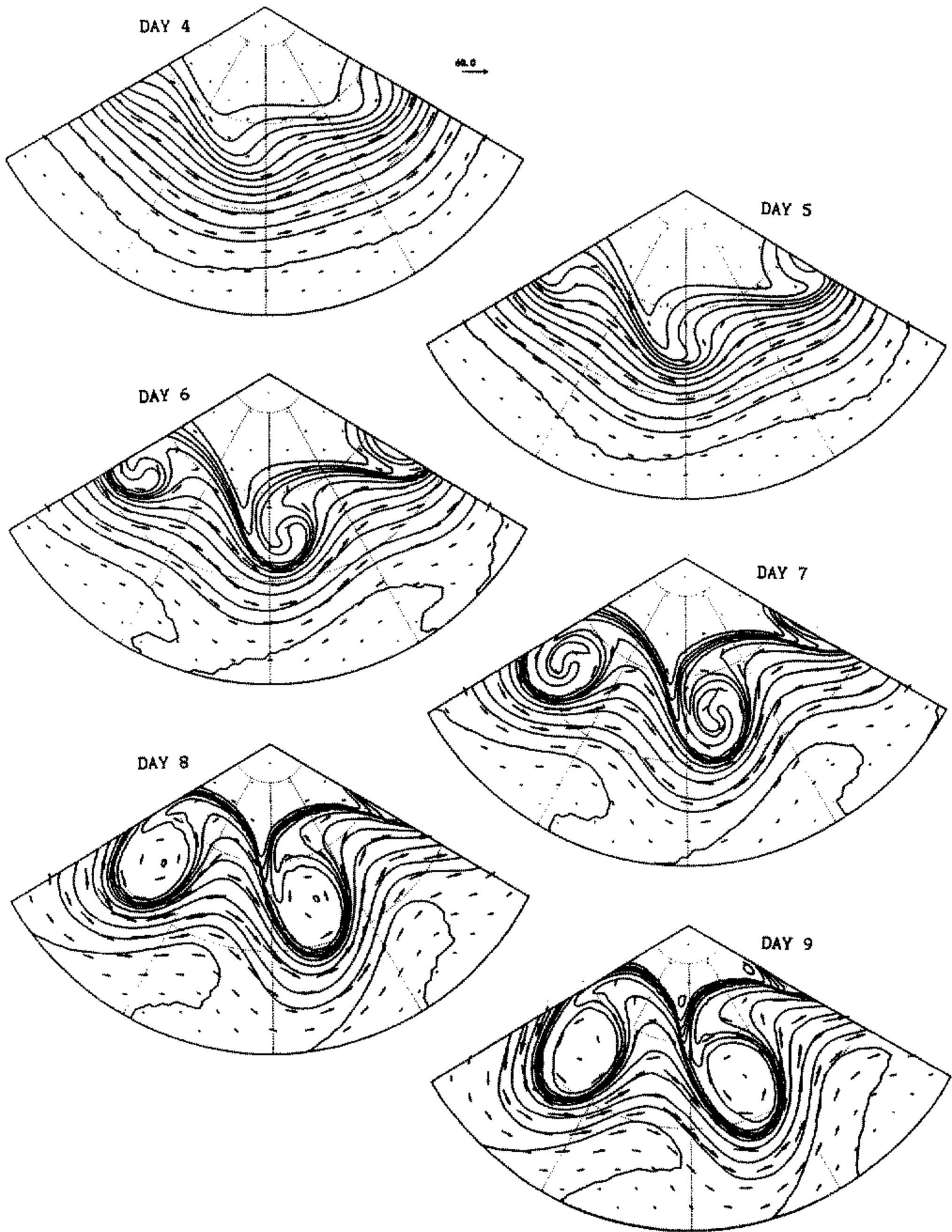


Figure 10. Potential temperature on the  $PV = 2$  PVU surface in LC2 between days 4 and 9. Contours are drawn every 5 K from 290 K to 350 K going equatorward, except that on day 9 model hyperdiffusion has produced additional small closed 285 K contours near  $70^\circ\text{N}$ . Wind vectors are included; for days 4 to 7 these have had the phase speed of the normal mode removed to give the relative flow. The arrow scale is as in Fig. 11 (with allowance for the different figure dimensions). Sectors are shown for two wavelengths between latitude  $20^\circ\text{N}$  and the pole. Lines of constant latitude and longitude are drawn every 20 and 30 degrees, respectively.



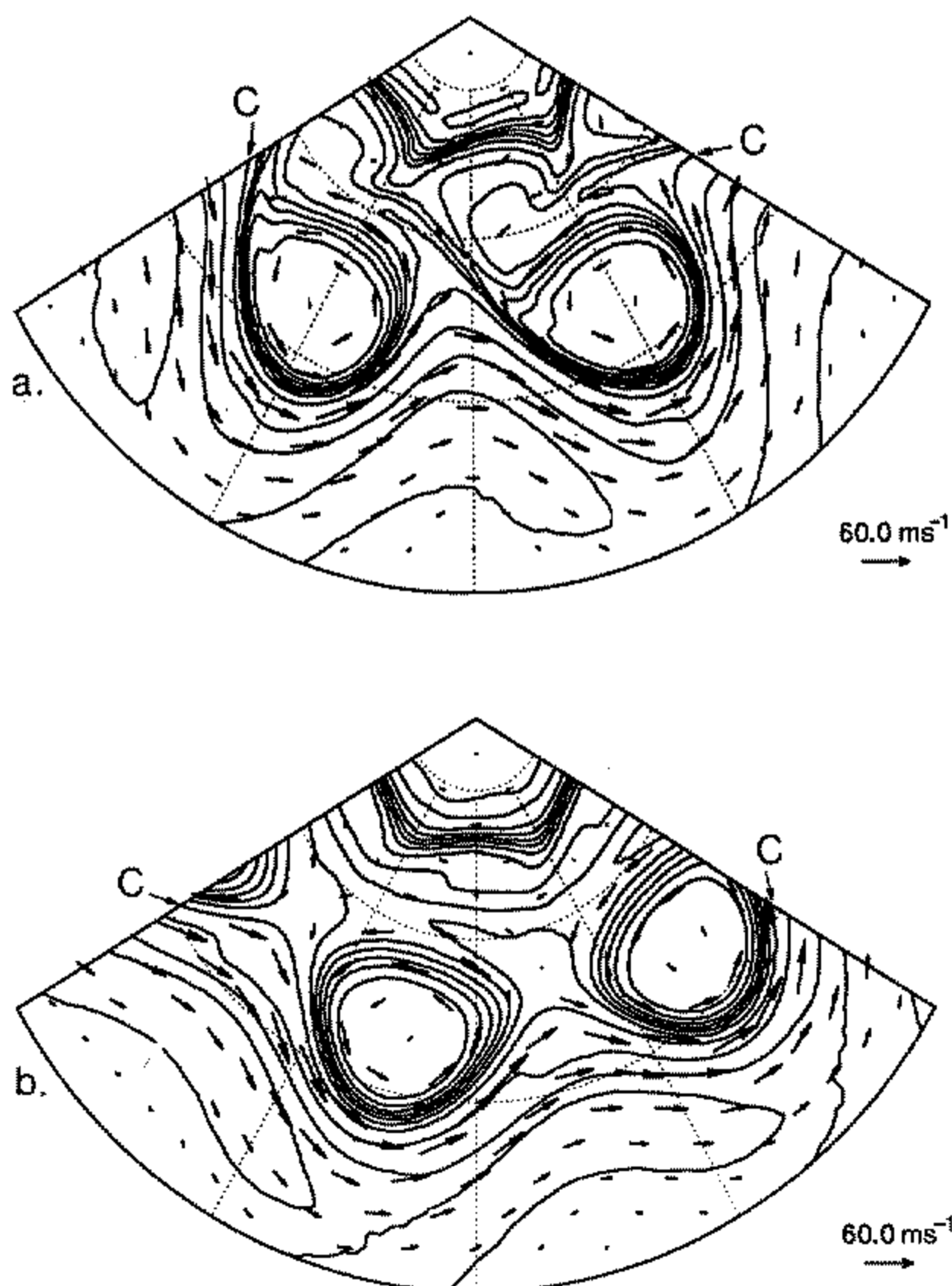


Figure 11. Potential temperature on the  $PV = 2$  PVU surface in LC2 for (a) day 11 and (b) day 15. Plotting conventions are as for day 9 in Fig. 10; in (b) the 285 K contours produced earlier by hyperdiffusion have reconnected into two nearly-zonal contours. The undular contour marked CC has the value 335 K.

to present a kind of partial barrier to the wave in LC2, though not in LC1. We return to this point near the end of section 9.

### (b) *Two Atlantic storm-track scenarios*

Figure 12 shows schematically two examples of  $\theta$ -contours on the  $PV = 2$  surface (equivalently, the  $PV = 2$  contour on a  $\theta$ -surface) indicating counterparts to the two different evolutions shown above, as they might occur across the North Atlantic. Both scenarios envisage the initiation of the baroclinic wave near the east coast of the North American continent by a surge of low- $\theta$  air from polar regions. This air will tend to tilt into the jet in a NW–SE direction, as seen in both life cycles and in the trough at  $50^\circ\text{W}$  in Fig. 2. Note that, since both troughs are initially located north of the mean jet maximum, the two life cycles start similarly. Crucial differences become apparent during the cyclonic wrap-up stage of the life cycle, in which trajectories are predominantly cyclonic in the manner of branches B and C in Fig. 1. During this stage, some high- $\theta$  subtropical air tends to be wrapped up with the low- $\theta$  polar air in the trough.

In the LC1-type scenario (early cyclonic and late anticyclonic behaviour, Fig. 12(a)), there are strong equatorward excursions during the cyclonic wrap-up stage, as the trough penetrates through the mean zonal jet maximum and becomes affected by the mean

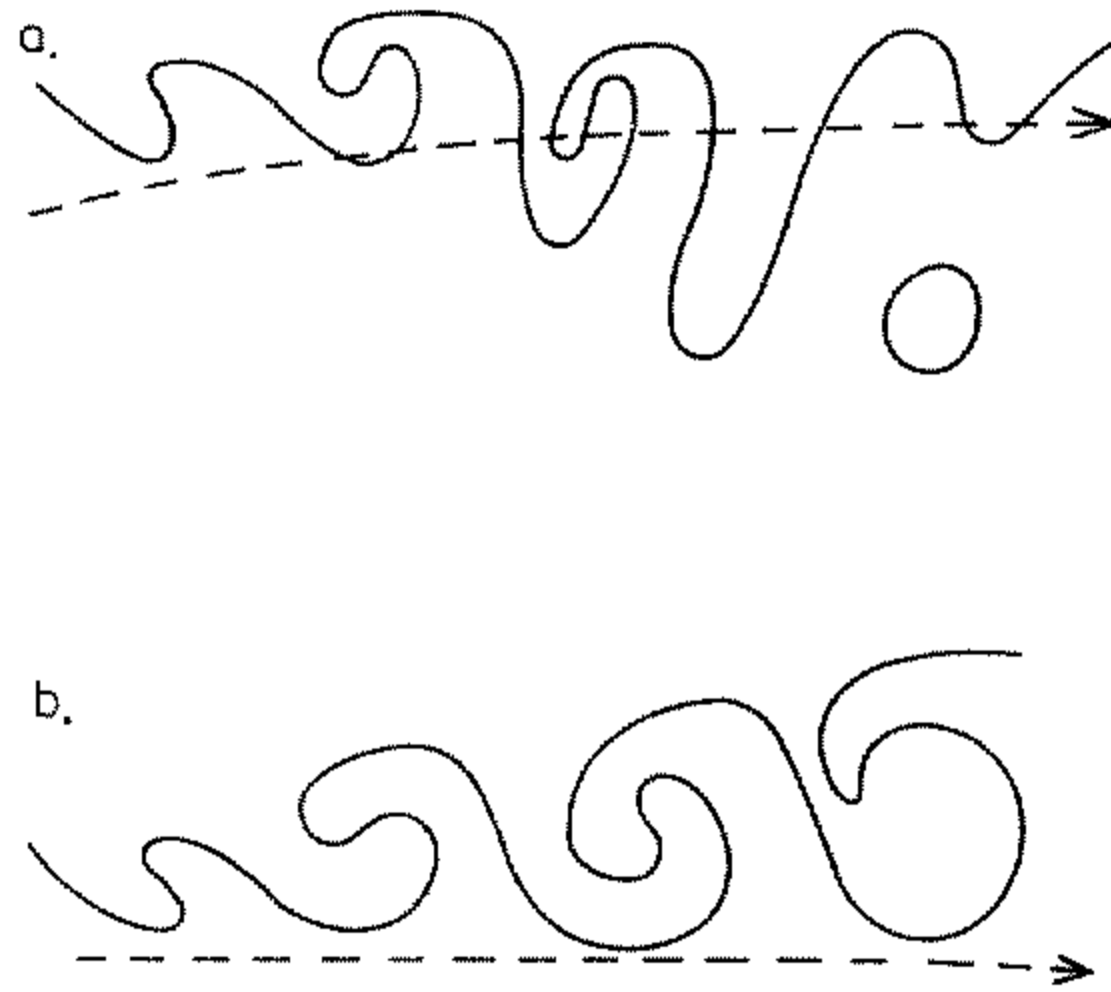


Figure 12. Schematic of a PV- $\theta$  contour in an Atlantic storm track sharing its main characteristics with (a) an LC1-type life cycle and (b) an LC2-type life cycle. The dashed line marks the approximate position of the mean jet at each stage.

anticyclonic shear. The trough then tilts in the NE–SW direction with this shear south of the mean jet. The trough thins and may eventually produce one or more cut-off cyclones, often near the Iberian peninsula, where such cyclones are common. Figure 2 shows an example. Note that at day 9 in Fig. 7 only three  $\theta$ -contours have been cut off, and that the contours outside these are still connected to the polar region in the manner of an ‘umbilical cord’ or shear line. This has some similarities to cut-off phenomena seen in barotropic integrations like that of Jukes and McIntyre (1987). When contours are cut off, however, a new trough tip is left to the north, which may be active in secondary cyclogenesis. Indeed, from an examination of analyses done at the European Centre for Medium-range Weather Forecasts we have noticed that troughs moving off the American continent have also sometimes gone through a similar evolution, leaving a cut-off over the southern United States.

LC1 also has some features in common with events that occur during anticyclonic blocking situations. First, troughs, on approaching a block, often tend to tilt in the NE–SW direction. Then these troughs often become disrupted and produce a cut-off cyclone south of the block, while the new trough tip skirts to the north of the anticyclone; at the same time low PV from the subtropics is fed into the blocking anticyclone. This picture appears to be consistent with the theories of eddy reinforcement of blocking discussed by Illari and Marshall (1983), Shutts (1986) and Hoskins and Sardeshmukh (1987).

In the LC2-type scenario (cyclonic-type behaviour, Fig. 12(b)), there is less equatorward movement of the trough. The cyclonic wrap-up has a broader zonal scale and the trough remains north of the mean jet. As in the LC1-type scenario, high- $\theta$  air is advected into the trough from the poleward moving cyclonic branch C in Fig. 1. Hyperdiffusion in the model tends to destroy any small-scale  $\theta$ -gradients within the trough. However, strong gradients do remain at the edges of the vortex, as discussed in the previous section. Note that there is no thinning of the trough, nor production of a small-scale cut-off. The only cutting off that occurs during this life cycle arises through hyperdiffusion to the north-west of the vortex, as clearly seen at day 15 in LC2 (Fig. 11(b)). This results in a large-scale cut-off and has some similarities to the type of

barotropic vortex roll-up long familiar in classical aerodynamics (e.g. HMR, Fig. 22) as well as to the real-atmospheric case of Fig. 5 of HMR. It is of interest to note that, in the cyclonic-type life cycle LC2, a cut-off anticyclone does not form. This suggests that it is wrong simply to think of the cyclonic and anticyclonic types of life cycle as opposite to each other. Further insight into why this is so will emerge in sections 7–9.

(c) *Trough thinning and broadening*

It has been mentioned several times in the discussion that the upper-air LC1 trough thins in the mean anticyclonic shear, whereas the LC2 trough broadens in the cyclonic shear. Experience suggests that this is a dynamically robust effect, in the sense that it depends only on the broad qualitative features of the situation. The impression of robustness is reinforced by a simple argument using ‘PV thinking’. Consider an initial large-scale sinusoidal Rossby wave with flow approximately parallel to the contours, as in Fig. 13(a). A tilt in the NE–SW direction, characteristic of a trough in mean anticyclonic shear, can be thought of as a smaller-scale dipolar PV pattern superimposed on the sine wave, as suggested by the plus and minus signs in Fig. 13(b). Because of the smoothing properties of the PV-inversion operator, what HMR call the ‘scale effect’, the wind field resulting from the inversion of such a PV distribution will be dominated by the large-scale PV field and will be more nearly sinusoidal than the new PV distribution itself. As suggested by the two arrows in Fig. 13(b), this results in more cross-contour flow in the rear of the trough, and flow more parallel to the contours ahead. Thinning of the trough is therefore to be expected and, again, because of the scale effect, so is further tilting in the NE–SW direction, as the thinned trough behaves increasingly like a passive tracer.

Figure 13(c) shows an experiment following the same line of thought except that the trough is sheared cyclonically. In this case the scale effect results in a cross-contour flow that broadens the trough. We therefore expect broad troughs on the cyclonic side of the jet and thin ones on the anticyclonic side (and of course vice versa for ridges). Furthermore, the scale effect makes a broad trough more dynamically active, and hence more

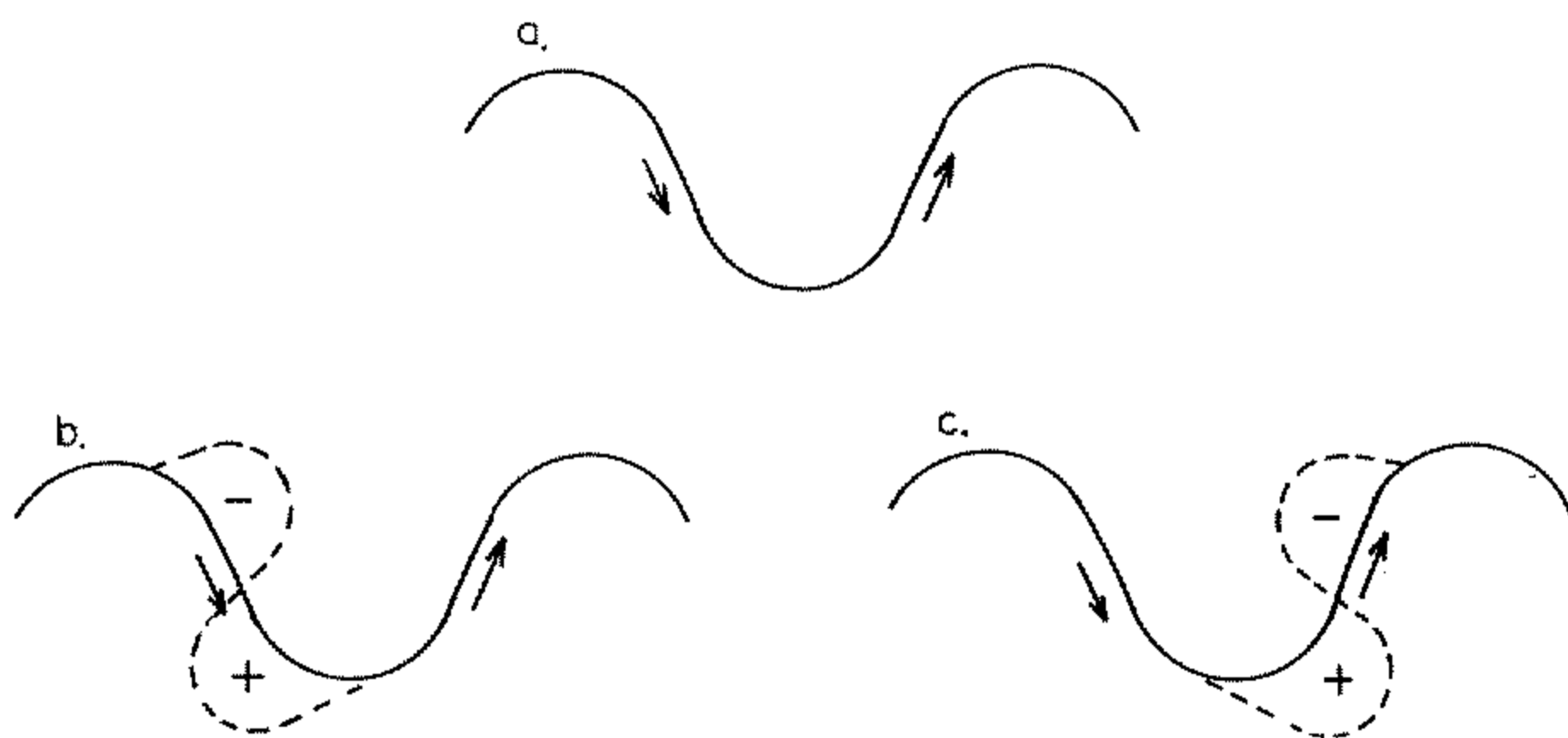


Figure 13. A thought experiment indicating the effects of meridional shear on the evolution of an initially sinusoidal PV-theta contour: (a) indicates a contour with implied winds before the meridional wind shear has tilted it. The dashed contours in (b) and (c) represent the configuration resulting from anticyclonic or cyclonic tilting, respectively (see text).

capable of wrapping itself up. This is in agreement with the results presented above and with other idealized studies (e.g. Marcus 1990).

Note that in the model life cycles the mean jet and shear are oriented zonally, implying that a thinning trough, for example, will have a NE–SW orientation. In the Atlantic region, however, the jet often has a NE–SW orientation itself. The ideas discussed above are still valid, but in this case a thinning trough will have a more meridional orientation.

(d) *Another observed example showing both types of behaviour*

The following example is taken from UK fine-mesh analyses of  $\theta$  on the PV = 2 surface and occurred between 00 GMT on 27 Jan. 1990 and 00 GMT on 29 Jan. 1990 (see Fig. 14). The sections show  $\theta$  in degrees Celsius together with wind vectors. Values of  $\theta$  less than 50°C are shaded to emphasize the troughs. There is less contouring in the high- $\theta$  (unshaded) areas because these contain smaller-scale anomalies having little correspondence with any features seen in the idealized life cycles presented above. These may be associated with PV debris from earlier disturbances, or diabatic processes in the subtropical regions, or possibly data errors, and require further investigation.

At the beginning of this period, at 00 GMT 27 Jan. 1990 (Fig. 14(a)), the Atlantic is dominated by a large-scale ridge and trough. The trough, near longitude 20°W, is quite broad and has extended to below latitude 40°N by this time. It should be noted that there is cross-contour flow behind the trough and flow more parallel to the contours ahead, which implies that the trough will thin, as in Fig. 13(b). This has become more evident by 12 GMT 27 Jan 1990 (Fig. 14(b)) and, together with the tilt of the trough, is suggestive of the anticyclonic behaviour discussed above. A comparison between Fig. 14(a) and Fig. 14(b) shows a rapid equatorward migration of the trough during this 12-hour period.

The next trough moving off the American continent has its leading edge over Newfoundland (*ca.* 57° W) on the left of Fig. 14(b) and, as in Fig. 2 and as was found during the initial stages of LC1 and LC2, it has a pronounced NW–SE tilt. As can be seen in Fig. 14(c), during the next 12 hours this air turns cyclonically as it moves eastwards. The trough in the eastern Atlantic continues to extend equatorwards and to thin.

By 12 GMT 28 Jan. 1990 (Fig. 14(d)) the two troughs in the  $\theta$  distribution show even more pronounced cyclonic and anticyclonic behaviour simultaneously, in the central and eastern Atlantic, respectively. The relatively deep equatorward penetration of the eastern trough is very clear. Finally, during the next 12 hours (see Fig. 14(e)) the central trough has continued to wrap up cyclonically, whereas the eastern one is producing a small cut-off, rather like that in LC1.

Clearly, despite the extra complexity of the real atmosphere, there are characteristics seen here that resemble those seen in the idealized life cycles.

## 7. WAVE-MEAN VIEWPOINT

### (a) *Motivation*

How can one gain further understanding of the anticyclonic versus cyclonic behaviour, of which the mature stages of LC1 and LC2 represent such striking examples along with real-atmospheric events like those of Fig. 14? One way is by diagnosing the life cycles using EP (Eliassen–Palm) cross-sections and associated concepts, alongside other concepts from wave-mean interaction theory. In particular, the ideas symbolized by Fig. 13(b, c) can be put into the context of recent work on the theory of Rossby-wave critical

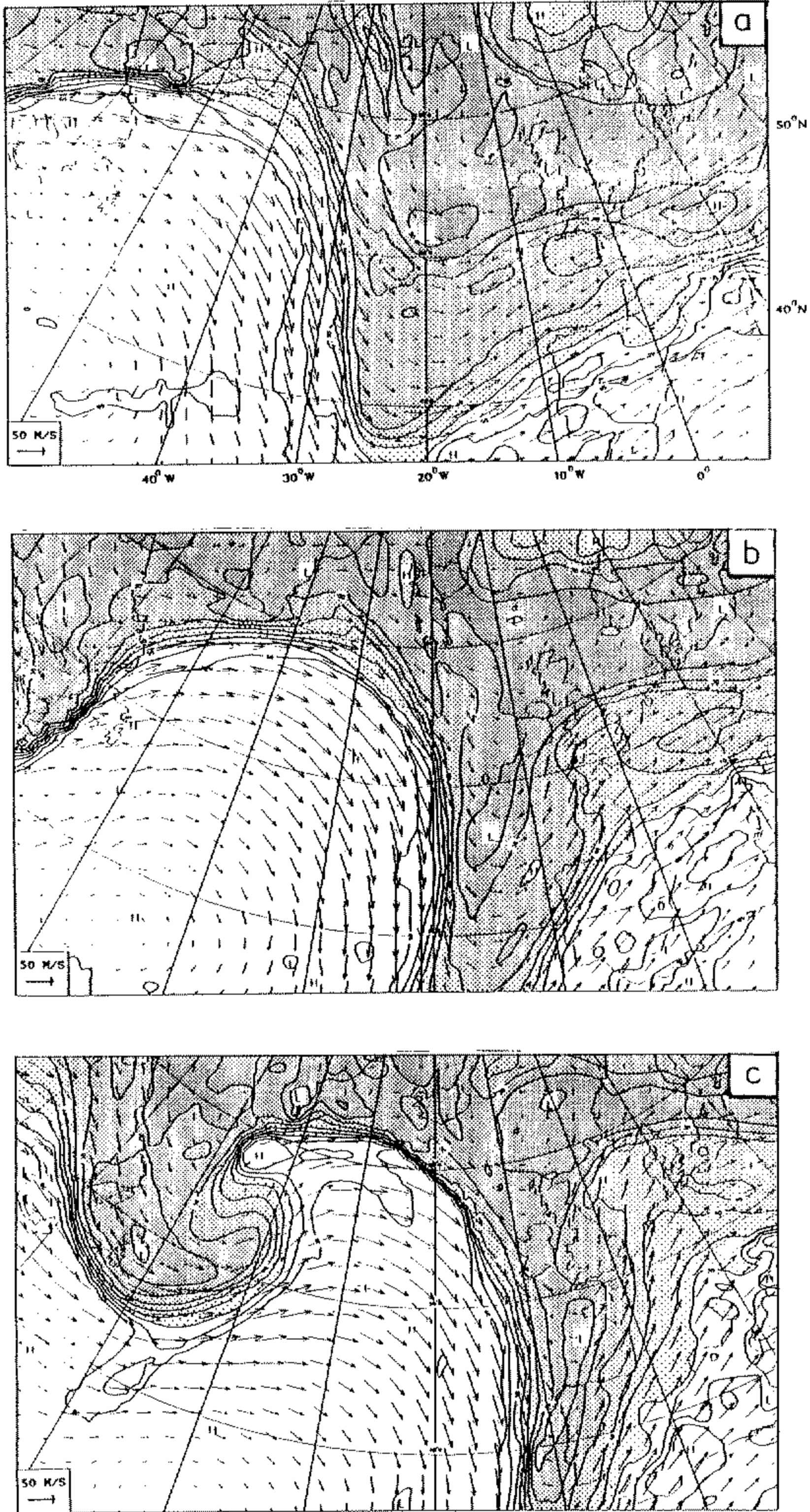


Figure 14. Potential temperature in degrees Celsius on the  $PV = 2$  PVU surface from the Meteorological Office's fine-mesh analyses at (a) 00 GMT 27/1/90, (b) 12 GMT 27/1/90, (c) 00 GMT 28/1/90 and (e) 00 GMT 29/1/90. Potential temperatures lower than  $50^{\circ}\text{C}$  are shaded with the lowest values shaded darkest. The contour interval is  $5^{\circ}\text{C}$ . Potential temperatures greater than  $60^{\circ}\text{C}$  are not contoured.

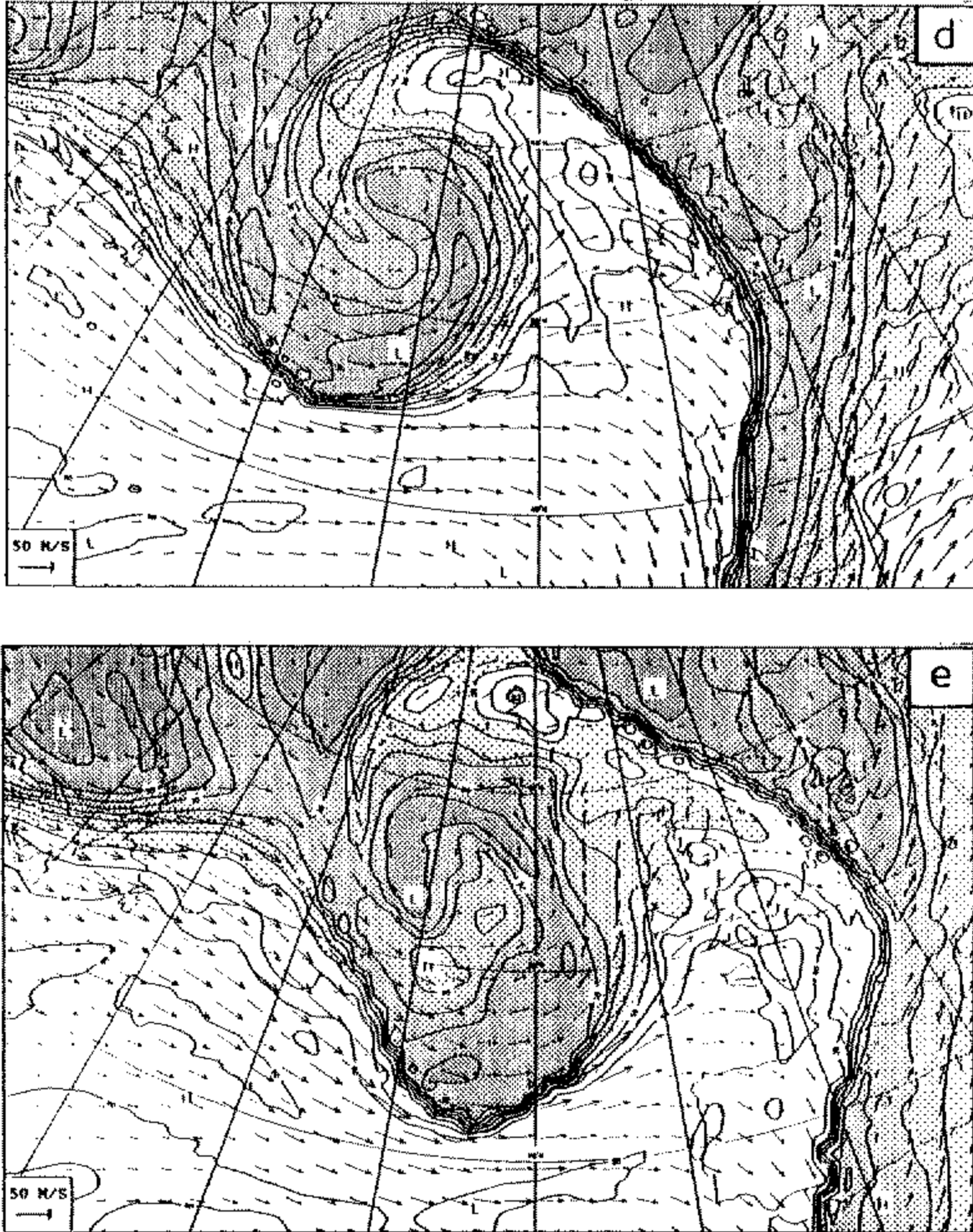


Figure 14. Continued.

layers and wave activity conservation relations. We now have a thorough understanding of the Rossby-wave nonlinear critical-layer problem itself (Haynes 1989) and considerable insight into generalizations beyond the restrictive parameter regime of critical-layer theory proper (see also the discussion in Killworth and McIntyre 1985, hereafter KM). The synthesis with the LC1 and LC2 diagnostics gives some important clues as to why, for instance, the two EKE curves in Fig. 4 are so different.

(b) *The EP flux vector*

For  $\beta$ -plane geometry the quasi-geostrophic EP flux vector is given in standard notation by

$$\mathbf{F} = \left( -\overline{u'v'}, \frac{f}{\theta_z} \overline{v'\theta'} \right) \quad (1)$$

where the two components refer to the meridional and vertical directions, and where subscript  $z$  represents the vertical derivative, with  $z$  either the geometrical or the pressure altitude, the overbar denotes a zonal average, and primes deviations from it. For further

details, and the extension to spherical geometry, see Edmon *et al.* (1980). The EP flux gives useful information about the momentum and heat fluxes in the life cycle and can be related to wave-action and group-velocity concepts. For small-amplitude disturbances we may define the associated wave activity density,  $A = \frac{1}{2} \overline{q'^2} / \overline{q}_y$ , where  $q'$  is the perturbation quasi-geostrophic PV and  $\overline{q}_y$  the usual quasi-geostrophic measure of the mean northward PV gradient. KM and Haynes (1988) give finite-amplitude counterparts to  $A$ , which remain well behaved even for small or zero  $\overline{q}_y$ , and to which we refer later. For adiabatic, frictionless, small-amplitude motion, we have the conservation relation

$$\frac{\partial A}{\partial t} + \nabla \cdot \mathbf{F} = 0. \quad (2)$$

Further, for small amplitude progressive waves with group velocity  $\mathbf{c}_g$ ,

$$\mathbf{F} = \mathbf{c}_g A \quad (3)$$

when the concept of group velocity is applicable, i.e. when ray theory applies. Thus  $\mathbf{F}$  gives a measure of the propagation of wave activity that is consistent with ray theory but more general.  $\mathbf{F}$  also gives the feedback to the mean zonal flow, as shown by the mean quasi-geostrophic PV equation:

$$\frac{\partial \overline{q}}{\partial t} = - \frac{\partial}{\partial y} (\overline{v'q'}) = - \frac{\partial}{\partial y} (\nabla \cdot \mathbf{F}) \quad (4)$$

where the generalized Taylor identity

$$\overline{v'q'} = \nabla \cdot \mathbf{F} \quad (5)$$

has been used. The EP diagnostics presented here, for days other than day 0, have been calculated after smoothing the model fields with a spectral filter, as was done by Hoskins (1980). A  $\nabla^{-4}$  filter was used with a constant chosen such that wavenumber 67 is reduced in amplitude by a factor 0.1. This allows the larger scales of the zonal mean to be seen more clearly, it being only such scales that are relevant to the ideas discussed above. The EP sections shown here were derived from formulae appropriate to spherical geometry, as given by Edmon *et al.* (1980). Inclusion of ageostrophic terms in the EP flux formulae, as given by Dunkerton *et al.* (1981), changed the amplitudes in Fig. 15 by an average of about 16% but changed the pattern of the smoothed fields very little; here we use the quasi-geostrophic forms.

### (c) *The saturation–propagation–saturation picture for wave-6 life cycles*

The starting point for this discussion is the fact, discovered by Edmon *et al.* (1980), that the time sequence of EP cross-sections for a lower-resolution version of LC1 exhibits what looks like a clear four-dimensional signature of free Rossby-wave propagation. The apparent propagation has a strong upward component, from the lower to the upper troposphere, and its EP signature is quite distinct from that of the linear baroclinic instability that begins the development. The four-dimensional signature, to be described and illustrated shortly, becomes apparent after the onset of the surface frontogenesis that marks the finite-amplitude saturation of the linear baroclinic instability wave, and hence the breakdown of linearized instability theory, around day 5.

For this and other reasons, including ideas from stratospheric dynamics, Edmon *et al.* took the process involved to be nonlinear radiation from a saturating instability, as discussed for instance by McIntyre and Weissman (1978). This interpretation was con-



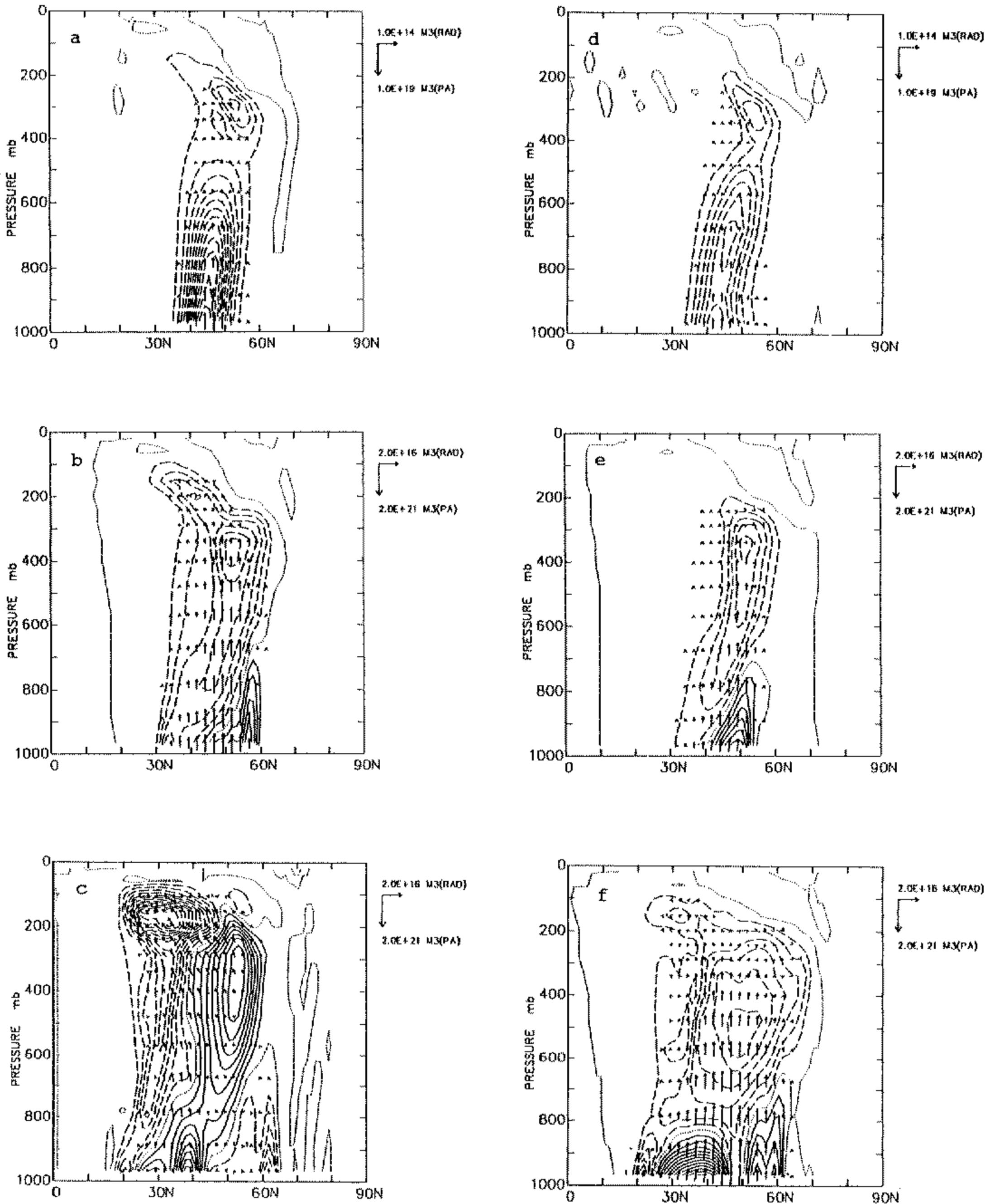


Figure 15. EP flux and its divergence during the two life cycles. (a), (b) and (c) are for days 0, 5 and 8 in LC1 and (d), (e) and (f) are for the same days in LC2. Dashed contours are negative and the contour interval is  $4 \times 10^{15} \text{ m}^3$ . The divergence in (a) and (d) has been multiplied by 400; note also the different arrow scalings (different by a factor 200), and recall that the surface pressure amplitude is 1 mb at day 0 and that the EP flux and divergence both scale with the amplitude squared. Units are as in Edmon *et al.* It should also be noted that these and subsequent sections overemphasize the vertical contribution to the EP vector because of the stretched ratio of vertical to horizontal scales.



firmed and further elucidated in the several subsequent publications mentioned in section 1. One interesting implication is that the greater part of the EKE build-up seen in Fig. 4, and the accompanying conversion of zonal available potential energy, for LC1, must be attributed not to baroclinic instability but, instead, to the free propagation of radiated Rossby-wave activity up into the strong upper-tropospheric westerlies. In other words the dynamics, from about day 5 onwards, becomes more like the well-known Charney–Drazin propagation of planetary-scale Rossby waves up into the stratospheric polar-night jet. This involves energy conversions that look superficially like those of baroclinic instability, but whose dynamical cause is quite different: for instance baroclinic instability, of the usual kind relevant here, depends on the existence of surface  $\theta$ -gradients, whereas upward Rossby-wave propagation does not.

The whole picture for LC1 and its predecessors can be summarized with reference to the horizontal dashed lines shown in Fig. 4, indicating four conceptually separate but temporally overlapping stages in the evolution, viz.

- (1) Exponential, normal-mode growth according to linear baroclinic-instability theory (valid roughly as far as day 4).
- (2) Nonlinear saturation in the lower troposphere, including the formation of fronts in the surface  $\theta$ -field (around day 5).
- (3) Upward propagation of Rossby-wave activity into the strongest mean westerlies, taking over from baroclinically unstable growth as the dominant cause of EKE increase (mainly days 5 to 7).
- (4) A second nonlinear saturation event in the upper troposphere and lower stratosphere (day 6 or 7 onwards).

It is this last saturation event, not the first one at stage (2), that is associated with the downturn of the LC1 EKE curve in Fig. 4. This last event involves the irreversible deformation of upper-air PV contours illustrated in Fig. 7, in which anticyclonic mean shear and the trough-thinning mechanism, symbolized by Fig. 13(b), have major roles. As remarked in earlier publications, this is essentially the kind of equatorward Rossby-wave ‘breaking’ that is also seen to take place, on a larger scale, in the wintertime middle stratosphere (e.g. Clough *et al.* 1985; McIntyre and Palmer 1984, 1985).

For brevity we shall refer to the whole picture as the ‘saturation–propagation–saturation’ or SPS picture of life-cycle evolution. It applies to all the wave-6 life cycles, published and unpublished, that we have diagnosed, with the proviso that LC2 and its lower-resolution counterpart reported as the ‘anomalous case’ by Simmons and Hoskins (1980) show even greater temporal overlap between the last three stages, as well as the very different upper-air morphology illustrated in Fig. 10. It can be seen from Fig. 10 that this upper-air morphology also involves irreversible PV contour deformation, but now occurring mainly on the poleward side of the jet, and dominated by cyclonic mean shear and the trough-broadening mechanism symbolized by Fig. 13(c).

The left half of Fig. 15 samples the time sequence of quasi-geostrophic EP cross-sections (after Edmon *et al.*) for LC1. Figure 15(a) is the linear normal-mode instability signature corresponding to stage (1) above. During stage (1) the spatial structure is time-invariant, the EP flux is convergent throughout the middle-latitude troposphere, and all quantities grow simultaneously and exponentially with time.

Figure 15(b, c) shows how, after the onset of stage (2), the structure rapidly becomes quite different from that associated with the linear normal mode. The difference is evident by day 5 (Fig. 15(b)). The tropospheric EP flux still has a strong vertical

component, but the convergence region is now concentrated in the upper troposphere and there now exists a divergent region above the surface. Furthermore the evolution between days 5 and 8 exhibits, increasingly clearly, the four-dimensional free-propagation signature already referred to, which originally led to the notion of a propagating stage of evolution. This signature consists of EP flux arrows pointing from a region of flux divergence to a region of flux convergence, the whole structure migrating approximately in the direction of the arrows, in this case upwards (seen clearly in Fig. 15(b)) and then equatorwards (see Fig. 15(c)), in the manner expected for a freely propagating Rossby wave packet. The wave-packet-like structure has become especially conspicuous around day 8; note the extensive trailing region of positive EP divergence in Fig. 15(c). It is likewise conspicuous in Fig. 3(c) of Edmon *et al.* The higher resolution of the present LC1 has changed some of the details and magnitudes—especially in the trailing divergence region, which on day 8 is nearly twice as strong here—but the gross features under discussion are the same. Note that if we fix attention at 400 mb and 53°N we see EP flux convergence on day 5 followed by divergence on day 8, as the apparent wave-packet structure migrates past that point. This corresponds to a reversal in the sign of  $v'q'$  there (see Eq. (5)). An idealized, linear-theoretic, progressive wave packet, involving purely undular PV contour behaviour, would exhibit all the features just described, including the reversal in the sign of  $v'q'$  as the wave packet propagates past a given point. As discussed by Held and Hoskins (1985), this behaviour of  $v'q'$  corresponds to PV contours, initially zonal, undulating and then straightening out again reversibly.

The wave-packet-like structure and upward migration is a much stronger indication of free upward Rossby-wave propagation than the orientation of the arrows on its own. As Fig. 15(a) illustrates, the latter is also a feature, for instance, of linear normal-mode instability (e.g. Edmon *et al.* 1980; HMR; Fig. 15(a, d) above). As Eady's instability theory illustrates, the vertical coupling involved in the instability can be entirely diffractive, analogous to quantum-mechanical tunnelling. In the present case there probably is, in fact, some free vertical propagation hidden in the upper-tropospheric normal-mode structure during stage (1) (see the refractive-index diagnostics below) but it is only after stage (2) of LC1 that the vertical-propagation signature asserts itself as a conspicuous feature. This is just what might have been expected from the arguments put forward by McIntyre and Weissman (1978) about the general properties of 'nonlinear radiation'.

The one-way propagation that appears to emerge around day 5, and to become a major feature by day 8, must depend on the absorption of a substantial fraction of the pulse of wave activity into the upper-tropospheric subtropics during stage (4). The upper subtropics seems able to drain the wave activity out of the jet region, like an anechoic lining in a small acoustic cavity. If this absorption were weaker, then wave activity would tend to be trapped in the cavity to a greater extent, and one would see less of a one-way propagation signature. For Rossby waves, the relevant concept of 'cavity' is that introduced in the stratospheric context by Matsuno (1970). Following Charney–Drazin and Matsuno, one might appropriately speak of a 'refractive-index cavity' in the upper troposphere; this will be further discussed in section 9. The relevant concept of 'absorption' is related to the concepts of nonlinear 'critical-layer absorption' and 'Rossby-wave breaking'. The idea that the upper-tropospheric subtropics is absorbing wave activity around day 8 is consistent with the PV morphology seen in Fig. 7. It resembles that of a nonlinear critical layer in its strongly absorbing stage, involving a substantial rate of irreversible rearrangement of the subtropical PV distribution. This is facilitated by the trough thinning mechanism (Fig. 13(b)), and by the relatively large area available on the tropical side of the jet—the whole picture illustrating the kind of poleward momentum flux that was once thought of in terms of a mysterious 'negative viscosity'.

*(d) The corresponding EP sequence for LC2*

The right-hand half of Fig. 15 shows the sequence of EP cross-sections for LC2. The linear-instability signature, and the early departure from it around day 5, have clear similarities to LC1. Since the early synoptic developments in LC1 and LC2 are also similar to each other, it seems reasonable to regard LC2 as having a stage (1) and a stage (2) that are similar to those of LC1 in all important respects. In particular, the EP flux is again convergent throughout the middle-latitude troposphere during stage (1). The changes due to the first onset of nonlinearity, marking stage (2), are again in evidence by day 5, and have much the same character. Like its counterpart for LC1, the EP cross-section for day 5 of LC2 (Fig. 15(e)) shows the emergence of a trailing region of EP divergence in the lower troposphere, again suggesting the upward launch of a Rossby-wave packet to initiate stage (3). After this, however, two major differences become apparent, contemporaneous with the growing differences in the synoptic developments.

The first difference is that the apparent propagation direction is oriented upward and to some extent poleward, rather than upward and strongly equatorward. This is consistent with the fact already noted that, in LC2, the strongest disturbance, as measured both by local EKE density and also by PV contour distortion, remains on the cyclonic side of the jet, rather than migrating to the anticyclonic side as in LC1. The second difference is that the subsequent development is less manifestly wave-packet-like. After what appears to be the initiation of free upward propagation, the EP cross-sections do not show the clear upward migration of a wave-packet-like signature.

It seems reasonable to suggest that, since these differences become apparent at a time corresponding to stage (3) of LC1, they are associated with different conditions in the upper half of the flow. Indeed they are just what one would expect for a cavity that is less absorptive. Note that, if an upward-propagating wave packet were to be reflected back downward early in stage (3), then the trailing EP divergence in the upward packet would tend to be cancelled by the leading convergence in the downward packet. Such a situation would also lead to a relatively persistent EKE, consistent with what is seen in Fig. 4. Appendix A gives more discussion of the EP fluxes in relation to the energetics.

In the next two sections it will be shown that the idea of a less absorptive cavity is consistent with the different upper-air morphology of LC2 together with a different refractive-index structure. Key points distinguishing LC2 from LC1 are (a) low refractive-index values together with the weakness of wave breaking and hence of absorption on the equatorward side, with PV contours behaving in a more undular manner in the jet region, and (b) the rapid decline in the rate of irreversible PV rearrangement on the poleward side, arising from the trough-broadening mechanism and the subsequent strong cyclonic wrapping-up in the more restricted area of the poleward region. This must make the poleward side, also, rapidly less absorptive, as will next be shown from wave-activity conservation principles.

## 8. NONLINEAR WAVE-ACTIVITY CONSERVATION

LC2's upper-air morphology (Figs. 10, 11) provides a remarkable example of approximately undular PV contours adjacent to regions where irreversible PV contour deformation takes place. On the equatorward side, such irreversible deformation as does take place does so in a region of much weaker PV gradients than in LC1. Because the gradients are weak, and the contour deformation less extensive, critical-layer theory predicts much less absorption in this situation. On the poleward side the same conclusion applies, but for very different reasons. By about day 15 (see Fig. 11(b)), substantial PV

rearrangement has ceased, leaving an almost steady pattern of vortices, where ‘steady’ means steady in some zonally-translating reference frame. Strictly speaking this is also an example of ‘wave breaking’ in the generalized sense relevant to wave–mean interaction theory (see McIntyre and Palmer (1985)) but, as will be seen, involving less wave-activity absorption than in LC1. Although rearrangement has been extensive, and the amplitude far too large to fall within the parameter regimes accessible to nonlinear critical-layer theory, our general understanding of that theory and its extensions forcibly suggests that, to the extent that PV rearrangement has ceased, the vortical region must also have developed low absorptivity. Such a picture is consistent with the EP cross-section for day 15 (not shown) which has EP fluxes close to zero everywhere.

The vortical region on the poleward side bears little detailed resemblance to any PV configuration encountered in critical-layer theory. Despite this, and despite the very different parameter regime, its non-absorbing character can be justified theoretically, as we now show using a theorem of Haynes (1988). Indeed the theorem shows at once that the PV configuration in the vortical region, i.e. northward of the main undular region bounded by the contour CC in Fig. 11, must be a non-absorber, in a well-defined sense, provided that this vortical region can be considered to have become a frictionless, adiabatic, steady flow.

If, conversely, the vortical or wave-breaking region is not steady, but is still bounded by undular PV contours like the contour CC, then the rate at which the region absorbs or re-radiates wave activity can be precisely related to a quantitative measure of the unsteadiness, namely the rate of change of the volume integral of the quantity  $\tilde{A}$  defined below. As will be explained, this rate of change is dominated by a certain measure of the rate of rearrangement of PV within the region. It defines the net absorptivity in a sense compatible with, but more accurate and more widely applicable than, that of Eq. (2),  $A$  being an approximation to  $\tilde{A}$ . These relationships comprise a significant extension of the work of KM on absorptivity bounds within the two-dimensional and the quasi-geostrophic three-dimensional context, showing more precisely how the general insights from nonlinear critical-layer theory extend far beyond the restricted parameter regime of that theory.

We assume, then, that the motion is adiabatic and frictionless, and consider the vortical region,  $V$ , say, to include the North pole and to be bounded above, below, and on the equatorward side by a material surface,  $\partial V$ , that is not deforming irreversibly. For definiteness one might for instance take  $\partial V$  to consist of isentropic surfaces above and below, and a near-vertical surface comprising undular PV contours on the equatorward side, like the contour CC in Fig. 11. Haynes’ theorem is now applied to the region  $V$ . The theorem is a finite-amplitude generalization of Eq. (2), expressed in isentropic coordinates  $(\lambda, \phi, \theta)$  where  $\lambda$  is longitude,  $\phi$  latitude, and  $\theta$  potential temperature as before, but now used as the vertical ‘coordinate’. It is a generalization not only in the sense that it holds for finite-amplitude disturbances, but also that it does not depend on the assumptions of quasi-geostrophic theory and, most importantly, does not depend on zonal or any other kind of averaging.

In place of Eq. (2) one has, for frictionless, adiabatic motion,

$$\partial \tilde{A} / \partial t + \nabla \cdot (\mathbf{u} \tilde{A} + \tilde{\mathbf{F}}) = 0, \quad (6)$$

where  $\nabla$  is the three-dimensional divergence operator and  $\mathbf{u}$  the horizontal wind vector. The wave-activity density  $\tilde{A}$  and the meridional and vertical components of its non-advective flux  $\tilde{\mathbf{F}}$ , to be defined shortly, reduce in the small-amplitude, quasi-geostrophic limit to the isentropic-coordinate counterparts of  $A$  and  $\mathbf{F}$  in Eq. (2). Explicit expressions are given below, but the most essential point can now be appreciated if we bring in one

more crucial piece of information, which distinguishes Haynes'  $\tilde{A}$  from other general, finite-amplitude measures of wave activity such as those arising in generalized Lagrangian-mean (GLM) theory (e.g. Andrews and McIntyre 1978). Unlike the GLM measures,  $\tilde{A}$  depends on the Eulerian fields only, if we suppose that the basic state has northward isentropic gradients of PV everywhere. Thus steadiness of the Eulerian fields within the region  $V$  implies steadiness of  $\tilde{A}$ . It follows at once that the total flux vector ( $\mathbf{u}\tilde{A} + \tilde{\mathbf{F}}$ ) is non-divergent. Furthermore, since the boundary  $\partial V$  of  $V$  is a material surface, the advective flux across it must vanish, and so it follows that the total non-advective flux across  $\partial V$ , namely

$$\iint_{\partial V} \tilde{\mathbf{F}} \cdot \mathbf{n} \, dS,$$

must also vanish, where  $\mathbf{n}$  is the inward normal in isentropic-coordinate space. If  $\partial V$  is an undular as well as a material surface then  $\tilde{\mathbf{F}}$  can reasonably be identified as the flux of wave activity due to wave propagation across  $\partial V$ , as distinct from advection, and the volume  $V$  can be said to be a non-absorber.

More generally, we have, from the divergence theorem in isentropic coordinates, the following expression for the total non-advective flux across the material surface  $\partial V$  into the vortical region:

$$\iint_{\partial V} \tilde{\mathbf{F}} \cdot \mathbf{n} \, dS = \frac{d}{dt} \iiint_V \tilde{A} \, dV. \quad (7)$$

This still depends on the assumption of adiabatic and frictionless motion, but not on steadiness since  $\partial V$  is a moving material surface. The advective flux is implicitly accounted for by the differentiation with respect to time on the right-hand side,  $V$  being a moving material volume.

Finally, the definitions of  $\tilde{A}$  and  $\nabla \cdot \tilde{\mathbf{F}}$  are as follows:

$$\begin{aligned} \nabla \cdot \tilde{\mathbf{F}} = & \frac{\partial}{a \partial \lambda} \left\{ -\frac{1}{2} \sigma_0 (u_c^2 - v_c^2) - \tilde{\alpha}(p_c, p_0, \theta) \right\} \\ & + \frac{1}{a \cos \phi} \frac{\partial}{\partial \phi} \left\{ -\sigma_0 v_c u_c \cos^2 \phi \right\} + \frac{\partial}{\partial \theta} \left\{ g^{-1} p_c a^{-1} M_{e\lambda} \right\} \end{aligned} \quad (8a)$$

$$\tilde{A} = -\sigma_c u_c \cos \phi + \sigma \int_0^{P_c} (P_c - \hat{P}) \frac{\partial Y}{\partial \hat{P}} (P_0 + \hat{P}, \theta) \, d\hat{P} \quad (8b)$$

where

$$\tilde{\alpha}(p_c, p_0, \theta) = g^{-1} \int_0^{P_c} \hat{P} \frac{\partial^2 H}{\partial \hat{P} \partial \theta} (p_0 + \hat{P}, \theta) \, d\hat{P}, \quad (8c)$$

and where  $a$  is the earth's radius,  $\phi$  the latitude,  $\lambda$  the longitude,  $\sigma$  the mass density in isentropic coordinate space,  $u$  and  $v$  the zonal and meridional velocities respectively,  $M = gz + H$  the Montgomery potential,  $H$  the specific enthalpy,  $p$  the pressure,  $g$  the gravity acceleration, and  $P$  the (Rossby–Ertel) potential vorticity defined as  $\zeta_a/\sigma$  where  $\zeta_a$  is the absolute isentropic vorticity (e.g. HMR Eq. (9)).  $Y$  serves as a PV-based meridional coordinate, similar to that used by KM (see their Eq. (5.15)),  $2\pi a Y(P, \theta) \Delta \theta$  being the mass contained in a layer between  $\theta$  and  $\theta + \Delta \theta$ , in the basic state, and between the equator and the PV-theta contour corresponding to the given values of  $P$  and  $\theta$ . The basic state, marked by subscripts zero, is not the Eulerian-mean state, which at finite amplitude does not lead to any simple wave-activity theorem. The basic state

required here can be defined as the result of rearranging the PV frictionlessly and adiabatically to be zonally symmetric on each isentropic surface, so that in the life-cycle experiments it would be approximately equivalent to the actual initial state, rather than to the Eulerian zonal mean state at subsequent times. The subscript 'e' signifies the departure from the basic state, and not departures from the Eulerian mean, although the two categories become indistinguishable in the small-amplitude limit used in deriving Eq. (2). A variable with no subscript represents the departure plus the basic state.

If Rossby numbers are small, in an appropriate sense—more precisely, if fractional changes in absolute isentropic vorticity  $\zeta_a$  are small—then Ertel's theorem,  $DP/Dt = 0$ , shows at once that fractional changes in  $\sigma$  must be correspondingly small, since  $\sigma = \zeta_a/P$ . It can be shown from this that the first term in the expression (8b) for  $\tilde{A}$  is small, of the order of the Rossby number, in comparison with the second. This justifies the earlier assertion that 'the rate at which the region absorbs or re-radiates wave activity . . . is dominated by a certain measure of the rate of rearrangement of PV within the region'; this measure can now be seen to be the contribution to Eq. (7) from the second term in  $\tilde{A}$ . Note that this dominance depends only on the smallness of fractional changes in absolute isentropic vorticity  $\zeta_a$ , and not on the far more restrictive assumptions of quasi-geostrophic theory. It can be shown moreover that the second term of  $\tilde{A}$  is positive definite, like  $A$ , in the present situation where the basic state has northward isentropic gradients of PV everywhere. One can, in fact, think of this second term of  $\tilde{A}$  as a kind of sideways version of Lorenz' available potential energy (APE), in which the sideways PV rearrangement in the present situation corresponds, mathematically speaking, to the vertical entropy rearrangement considered in Lorenz' theory. Some further discussion of the analogy with APE is given by KM in their section 5.

It can be noted that the foregoing argument justifies, and makes precise, the heuristic idea that a steady vortical region cannot absorb Rossby waves without gaining vortical 'energy', nor radiate them without losing 'energy'. In fact ordinary energy is not a relevant quantity for this purpose; one reason is that we are dealing with wave propagation in a moving medium. It is wave-activity functionals like  $\tilde{A}$  that are relevant, and that can describe what it is that is lost or gained by, or exchanged between, the undular and vortical regions.

The possibility of steady-state configurations consisting of a large-amplitude undular region adjacent to a vortical region with, by implication, zero exchange of wave activity between them has often been demonstrated in the context of two-dimensional, inviscid vortex dynamics. A range of analytical solutions showing that such situations are dynamically possible (well beyond, as well as within, the confined parameter regime of critical-layer theory) have been given for instance by Stuart (1967) and Shercliff (1977). The mature stage of the most strongly nonlinear case studied in the barotropic numerical experiments of Held and Phillips (1987) is essentially the same kind of situation. Here, too, the vortical region, or rather regions (one on each side of an undulating jet region), have ceased to act as absorbers of wave activity once the wave-breaking process has brought about all the PV rearrangement it can. The central undulating region in the strongly nonlinear case of Held and Phillips provides us, in fact, with a very clear example of a conservative (non-absorptive) Rossby-wave cavity, such as might have been anticipated via insights from nonlinear critical-layer theory.

Equation (7) does not by itself rule out the possibility that the vortical region might at some later time re-radiate some of the wave activity it has absorbed. In the Held and Phillips and other cases cited this does not occur, presumably because they concern two-dimensional configurations in which there is nowhere else for the wave activity to go. It is likely (albeit less obvious) that the same is true of LC2 in some approximate sense.

To demonstrate this unequivocally, one would need to make quantitative use of (7) and (8), with suitable choices of  $V$  and  $\partial V$ , assessing in particular the possibility of absorption of wave activity downward into the surface  $\theta$  distribution. Such a quantitative investigation is beyond the scope of this paper, and is left for future work.

In connection with LC1, it is worth noting that the advective contribution,  $\mathbf{u}A$ , to the wave-activity flux in Eq. (6) must have a significant role. Here, and in stark contrast with LC2, the equatorward wave breaking and PV rearrangement is so massive that there are no PV contours whose behaviour comes close to being purely undular, even in the jet region. If the boundary of the jet region cannot be taken to be a material contour, then with such large amplitudes the advection of  $\tilde{A}$  across non-material boundaries must inevitably enter into the wave-activity accounting. In LC1 one might say that we have a sort of inextricable merging of equatorward wave propagation with equatorward wave breaking, just as in the large-amplitude stratospheric case.

As regards the equatorward side of the jet region in LC2, the EP cross-sections have already suggested a far weaker rate of absorption of wave activity into the subtropics. This is also understandable from the form of Eq. (7), together with the fact that the upper-air morphology is quite different from that of LC1. In the case of LC2 we can apply Eq. (7) to a region  $V$  between the southernmost undular contour and the equator; the point is that, although weak wave breaking does take place in that region, it does so well away from the strong isentropic gradients of PV marking the tropopause, and wholly within a region of weak isentropic gradients of PV in the subtropical troposphere. The consequence is a relatively small rate of PV rearrangement, hence a small right-hand side of the expression (8b), by comparison with LC1, implying comparatively weak absorption.

Finally, to complete the discussion, it is necessary to consider the region above the jet core. On examining the PV fields on high isentropic surfaces (not shown) it is found that some rearrangement of PV does occur in both life cycles. However, it appears that because  $\sigma$  in (8b) is smaller at these altitudes than near the jet core itself,  $\tilde{A}$  values and rates of change are correspondingly smaller and certainly less significant than on the equatorward side of the jet in LC1. The weak EP flux divergences above the jet in Fig. 15 are consistent with this conclusion, as are the relatively small values of  $\bar{q}_y$  above the tropopause in Figs. 16 and 17 (q.v. below).

## 9. REFRACTIVE INDEX DIAGNOSTICS

The subtropical wave breaking in LC2 is so weak that one might argue that ideas from linear wave theory are directly relevant on the equatorward side, as well as in the jet region itself, where the PV gradients are large but the PV contour behaviour undular to a remarkable extent—a fact that is connected with the larger intrinsic wave phase speeds on the anticyclonic side of the jet. We want to look at the linear-theoretic aspects for another reason also. We have seen strong circumstantial evidence for the role of upward Rossby-wave propagation in LC1 and, by inference, in LC2, but have not directly checked that this idea is actually consistent with Rossby-wave propagation theory. The two most important consistency checks are first to ask whether isentropic contours of PV behave in a sufficiently undular manner for the wave propagation mechanism to be able to operate at least qualitatively as in linear wave theory (e.g., HMR section 6(a), Fig. 17), and second to ask whether isentropic gradients of PV in the jet region are indeed of a sufficient order of magnitude to support the supposed propagation.

On the first question, wave-theoretic considerations suggest that conditions for undular behaviour are most likely to be satisfied where intrinsic phase speeds ( $c - \bar{u}$ ) are



largest in magnitude. This can be seen, for instance, from the results of critical-layer theory. It has already been emphasized that in LC2 we have a remarkably clear example of PV- $\theta$  contours behaving in an almost purely undular manner in the upper-tropospheric jet, where  $|c - \bar{u}|$  is largest. Held and Hoskins (1985) discussed contour behaviour below the jet core in a lower-resolution version of LC1, and found that a PV contour close to 1 PVU on the 315 K  $\theta$ -surface was apparently undular, with a behaviour that was 'nearly reversible' like that in the idealized theoretical wave-packet scenario mentioned in section 7(c). Meridional contour displacements,  $\eta(\lambda, t)$ , increased in stages (2) and (3) of the life cycle, and then decreased in stage (4). As already pointed out in section 7(c), a reversible decrease in  $\eta$  is consistent with the appearance of the trailing EP divergence region near 400 mb and 53°N in Fig. 15(c).

However, the higher resolution used in the present LC1 (T95 as compared with T42) reveals that all the relevant PV contours exhibit some irreversible deformation. With finer details thus included, the picture is not as clean-looking as that found by Held and Hoskins at lower resolution. For example, in the present study part of the 1 PVU contour on the 315 K surface is cut off irreversibly to the south. Such a feature was not found in the lower-resolution version which, with hindsight, must have been significantly affected by hyperdiffusion. In LC1 the remainder of the contour, to the north, still exhibits quasi-reversible behaviour, apparently enough to account for the EP divergence. It appears that there is sufficient undular behaviour in the jet region to allow us to retain the idea, already suggested by the four-dimensional EP signature, that Rossby propagation is important; the main modification in the present, high-resolution LC1 is to admit that some wave breaking and consequent dissipation of wave activity must be taking place almost everywhere, even in the jet region. Figure 7 illustrates this: by contrast with LC2 (Fig. 10), there is no contour in Fig. 7 whose behaviour is nearly undular; nevertheless, it remains true that in LC1 the most dynamically important irreversible contour deformation, and the most massive PV rearrangement, is taking place on the subtropical side of the jet.

On the second question, whether isentropic gradients of PV are of a sufficient order of magnitude to support the supposed propagation, the standard theories (e.g. Matsuno 1970) show that the answer depends sensitively on the intrinsic zonal phase speed ( $c - \bar{u}$ ) as well as on the isentropic gradients of PV that enable wave propagation to take place. According to quasi-geostrophic, linearized Rossby-wave theory, the PV gradients are sufficient if the size of the cavity is large enough in comparison with the earth's radius,  $a$ , divided by typical values of  $l$  where

$$l^2 = K^2 - m^2, \quad (9)$$

$m$  being the zonal wavenumber, an integer ( $m = 6$  in our case), and where

$$K^2 = \frac{a^2 \bar{q}_y}{u - c} \quad (10)$$

where  $\bar{q}_y$  is the relevant quasi-geostrophic measure of the basic northward isentropic gradient of PV, as expressed by the Charney-Stern relation (HMR [Eqs. 39a,b]) and as used in Edmon *et al.* [Eq. 3.8, multiplied by  $a^{-1}$ ]. Sometimes it is preferable to work with  $K$  or  $K^2$ , rather than  $l^2$ , so as to be able to plot cross-sections that apply to more than one zonal wavenumber; it is  $K$  that is plotted here. However,  $l$  is the true refractive index, real values of which correspond to real meridional and vertical wavenumbers, and real group velocities, when ray theory is valid.

Figure 16 presents plots of  $K$  (on the left) and  $\bar{q}_y$  (on the right) for days 0 and 5 of LC1. Figure 17 presents the same information for LC2. The values of  $c$  used in the



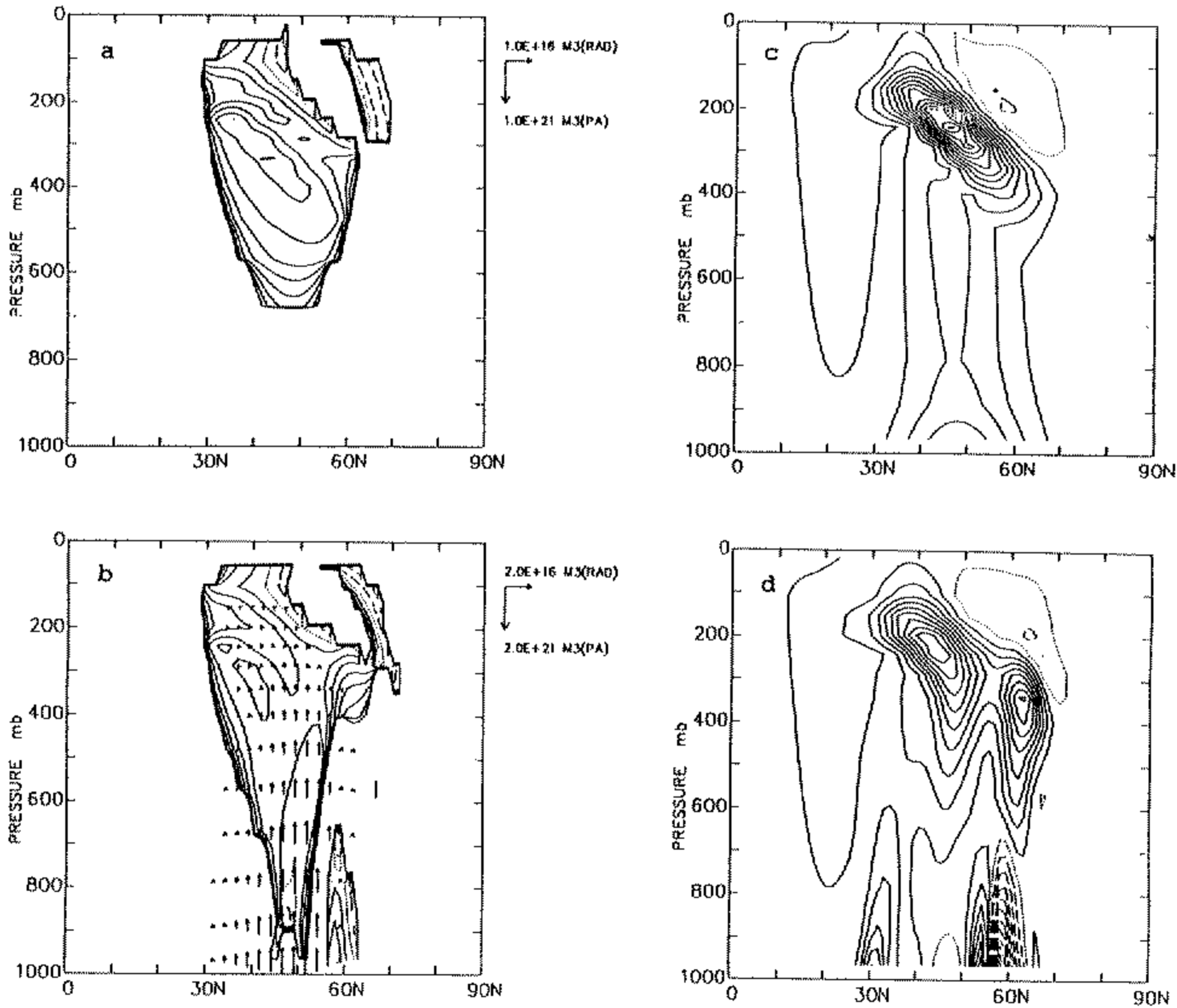


Figure 16. The modified refractive index  $K$ , or dimensionless 'total wavenumber', with EP flux vectors and  $\bar{q}_y$  in LC1. Only positive values of  $K$  are plotted. (a) and (b) show  $K$  for days 0, 5 and (c) and (d) show  $\bar{q}_y$  for the same days. The contour interval for  $K$  is 2, the dotted line represents  $K = 6$  and dashed lines  $K$  values less than this.  $K$  takes the value 6.2 in the upper central minimum discussed in the text and marked by a minus sign; the largest contour value in the tropopause ridge, just above, is 12. The contour interval for  $\bar{q}_y$  is  $2 \times 10^{-11} \text{ s}^{-1} \text{ m}^{-1}$ ; the dotted contour is 0 and dashed contours are negative.

calculation of  $K$  are those for the normal mode; a brief discussion of the applicability of this is given in Appendix B.  $K$ -values less than 6, corresponding to imaginary  $l$ , are shown by dashed contours, with  $K = 6$  ( $l = 0$ ) shown dotted. The main point to notice is the presence of substantial regions in which  $K$  does exceed 6. For instance the  $K$  values in Fig. 16(a,b) are of the order of 8 or more in much of the hypothesized upper-tropospheric cavity region, implying  $l \geq (8^2 - 6^2)^{1/2} \geq 5$ , hence  $a/l$  values corresponding to about 10 degrees latitude or less, i.e. latitudinal half wavelengths about 30 degrees latitude or less. These values, and their spatial extent, seem consistent with the notion that there is room for propagation, albeit not by a large margin. This judgement is supported by the fact that wave-9 life cycles (unpublished results, omitted for brevity) tend, by contrast, not to exhibit a discernible stage (3) at all, consistent with the fact that they have refractive-index cavities that are effectively too small, even though  $K$  does reach values exceeding 9 here and there.

Figure 17(a, b) also shows an extensive upper-tropospheric region where  $K$  exceeds 6, but not by as great a margin as in Fig. 16(a, b). Note the relatively broad region with  $K < 8$ , and the dotted  $K = 6$  contour indicating a deeper minimum, near 250 mb and 35°N, and a small region of imaginary  $l$ . The minimum  $K$  value is just above 5. The

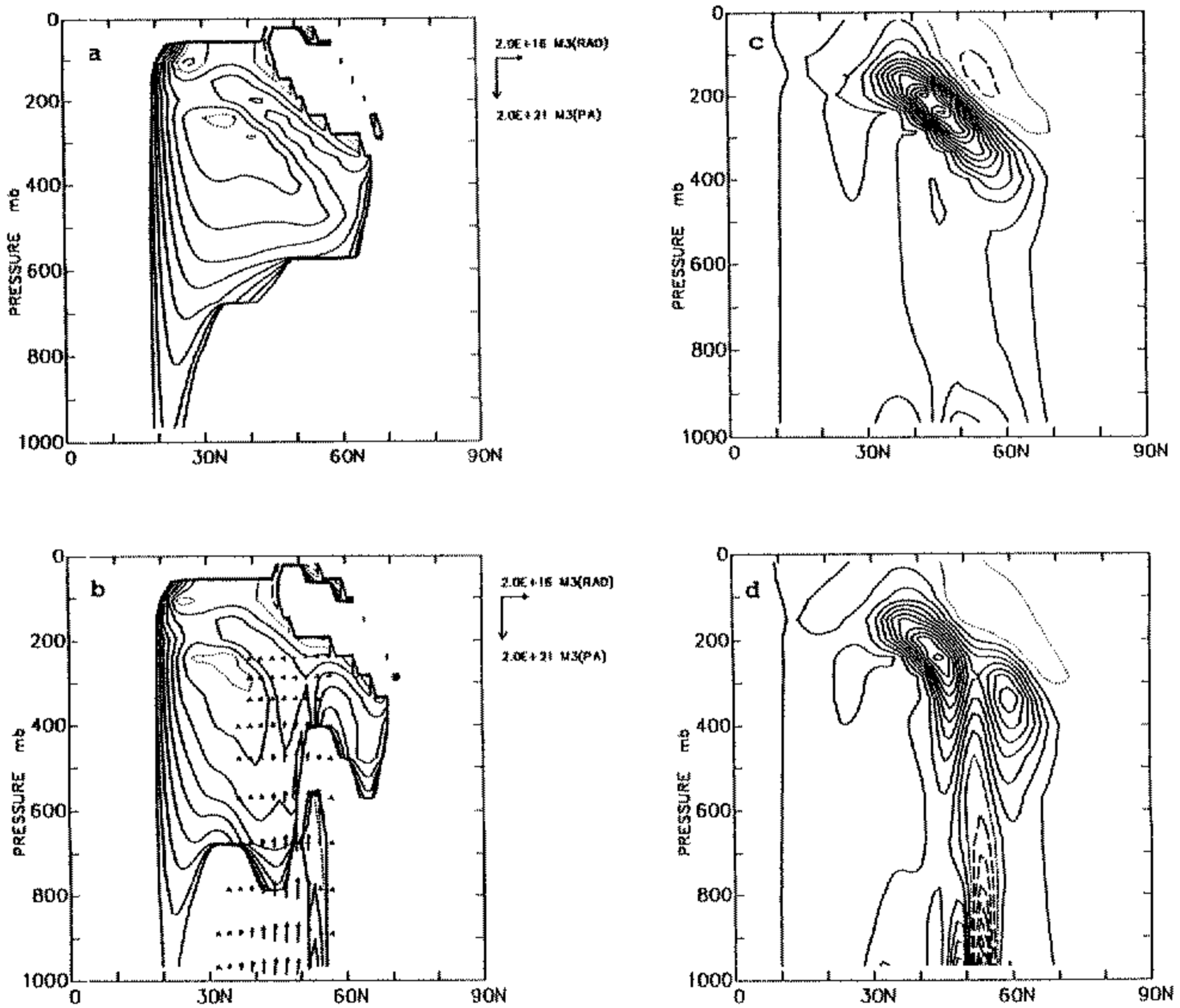


Figure 17. The modified refractive index  $K$ , or dimensionless 'total wavenumber', with EP flux vectors and  $\bar{q}_y$  in LC2. Only positive values of  $K$  are plotted. (a) and (b) show  $K$  for days 0, 5 and (c) and (d) show  $\bar{q}_y$  for the same days. The contour interval for  $K$  is 2, the dotted line represents  $K = 6$  and dashed lines  $K$  values less than this.  $K$  takes the value 5.1 in the upper central minimum discussed in the text and the largest contour value in the tropopause ridge, just above, is 12. The contour interval for  $\bar{q}_y$  is  $2 \times 10^{-11} \text{ s}^{-1} \text{ m}^{-1}$ ; the dotted contour is 0 and dashed contours are negative.

counterpart of this  $K$  minimum in LC1, as marked by the minus sign in Fig. 16(a) near 350 mb and  $40^\circ\text{N}$ , is a shallower and thinner feature with  $l$  remaining real. The broader and deeper  $K < 8$  region in LC2 is a direct consequence of adding cyclonic shear. This acts to increase the denominator  $(\bar{u} - c)$  on the right-hand side of (10), while hardly affecting the numerator  $\bar{q}_y$ .

The minimum in LC1 becomes shallower still by day 5 (see Fig. 16(b)). By examining the  $\bar{q}_y$  cross-sections in Fig. 16(c, d), it can be seen that this shallowing is a consequence of increased  $\bar{q}_y$  in the region where previously there were only small values of  $\bar{q}_y$ . The fact that  $\bar{q}_y$  does increase in this region can be understood by applying Eq. (4) to the EP flux pattern in Fig. 15(a, b). There is a similar affect in LC2, but the denominator  $(\bar{u} - c)$  in (10) still prevails, so that the  $K < 8$  region in LC2 remains broader and deeper than in LC1, throughout days 0–5 at least.

Comparison of Fig. 16(c, d) with Fig. 17(c, d) shows that LC1 and LC2 have very similar distributions of  $\bar{q}_y$  up to day 5. Besides affecting  $K$  itself, the increased  $(\bar{u} - c)$  in LC2 also promotes undular behaviour near the  $K$  minimum, as already implied, consistent with a displacement of the subtropical critical line  $\bar{u} - c = 0$  away from the region. The location of that critical line can be seen in Fig. 16(a, b) and Fig. 17(a, b) as the equatorward

edge of the plotted positive- $K$  contours, nearer  $20^\circ\text{N}$  in Fig. 17(a, b) as compared with  $30^\circ\text{N}$  in Fig. 16(a, b). Since undular behaviour again suggests some relevance for linearized wave dynamics, it is arguable that the  $K$  minimum acts somewhat like a diverging lens, refracting wave activity away from itself (e.g. Karoly and Hoskins 1982), even though simple ray-theoretic refraction or ‘geometrical optics’ is not a quantitatively valid concept here. There must, for instance, be some diffractive tunnelling of wave activity through the  $K$  minimum. Nevertheless, the  $K$  minimum, together with the weak  $\bar{q}_y$  values to its equatorward side, is probably part of the reason why the wave activity is deflected more poleward in LC2 than in LC1. In particular, the EP flux vectors for LC1 point upwards and then equatorwards towards increasing values of  $K$ , whereas the EP flux vectors for LC2 remain mostly to the north of the  $K$  minimum (Fig. 15). This minimum may therefore represent the ‘partial barrier’ alluded to in section 6(a).

This guiding of waves away from such refractive-index minima is a discernible effect, well known in classical physics, even when ray theory is not justifiable. One might count the effect as perhaps one of those phenomena that are sufficiently robust for the predictions of ray theory to survive outside the regime of validity of that theory. Strict validity requires that the size of the cavity, and the scales of refractive-index variations, be much larger than the earth’s radius  $a$  divided by  $l$ ; such a condition is not satisfied here.

Another such effect may be the tendency of the tropopause to act as a waveguide, often remarked on in the literature and suggested here by the sloping  $K$  maximum near the tropopause where  $\bar{q}_y$  is large. The EP diagnostics for stages (2) and (3) seem consistent with this idea also, although we need to remember when and where advective nonlinearity is strong, as it is to an overwhelming extent in the subtropical upper troposphere in LC1. There, in effect, equatorward advection takes over from equatorward propagation; this is expressed by the important role, already mentioned, of the advective contribution,  $\mathbf{u}\bar{A}$ , to the finite-amplitude wave-activity flux in Eq. (6).

#### ACKNOWLEDGEMENTS

This work was supported by the Natural Environmental Research Council through a post-doctoral fellowship to C. D. Thorncroft and through the U.K. Universities’ Global Atmospheric Modelling Project. M. E. McIntyre’s research received additional support through the U.S. Navy. We also thank P. H. Haynes, I. M. Held and A. O’Neill for many invaluable discussions, K. Spiers for help with some of the diagrams and the Joint Centre for Mesoscale Meteorology at the University of Reading for providing the data for Figs. 2 and 14.

#### APPENDIX A

##### *The EP fluxes and their relation to the energetics*

It is well known from classic theories of stratospheric planetary-scale Rossby-wave propagation (Charney and Drazin 1961; Matsuno 1970; Andrews *et al.* 1987) that, with northward isentropic gradients of PV, Rossby waves propagating upwards into westerly mean winds that increase with altitude will always give rise to positive baroclinic conversion from zonal available potential energy into eddy energy. This is because upward EP fluxes correspond to poleward eddy heat fluxes, and because positive mean thermal winds correspond to equatorward mean isobaric gradients of temperature and potential temperature. These two facts constrain the energy conversion to be positive, in the

familiar way. The positive energy conversion is consistent, also, with the behaviour of 'wave action' and other conservative measures of wave activity (e.g. Gill 1982 section 8.12.5; Haynes 1988), as intrinsic frequencies and phase speeds increase in magnitude through propagation into stronger mean winds. These considerations, taken together with the breakdown of linear theory after stage (1), justify the notion of 'upward propagation . . . taking over from baroclinically unstable growth as the dominant cause of EKE increase' during stage (3).

In the same way equatorward EP fluxes, conspicuous at day 8 in LC1, correspond to EKE decrease through barotropic conversions. This is because equatorward EP fluxes correspond to poleward momentum fluxes, and because they are on the equatorward flank of the mean zonal jet. Thus, the predominantly vertical EP fluxes in the first half of LC1, and the more horizontal EP fluxes later, correspond well to the rise and fall of EKE shown in Fig. 4.

## APPENDIX B

### *Variations of the phase speed and linear growth rate with time*

The choice of  $c$  is important in the calculation of  $K$ . In the present study this has been taken to be the phase speed of the most unstable normal mode. The relevance of this value at the time when free vertical propagation of Rossby waves is most pronounced, starting around day 5, might be questioned. Figure B.1 indicates the phase speed, as given by a single vorticity coefficient, for LC1 at  $\sigma = 0.287$  and  $\sigma = 0.967$ . This is the largest spectral coefficient at day 0, and peaks at these upper and lower levels. The phase speed for the normal mode is 11.9 degrees longitude per day. The upper wave and lower wave propagate with this speed for the first few days, but after day 3 the upper wave accelerates whilst the lower wave decelerates, as growth rates begin to depart from their normal-mode values (see Fig. B.2).

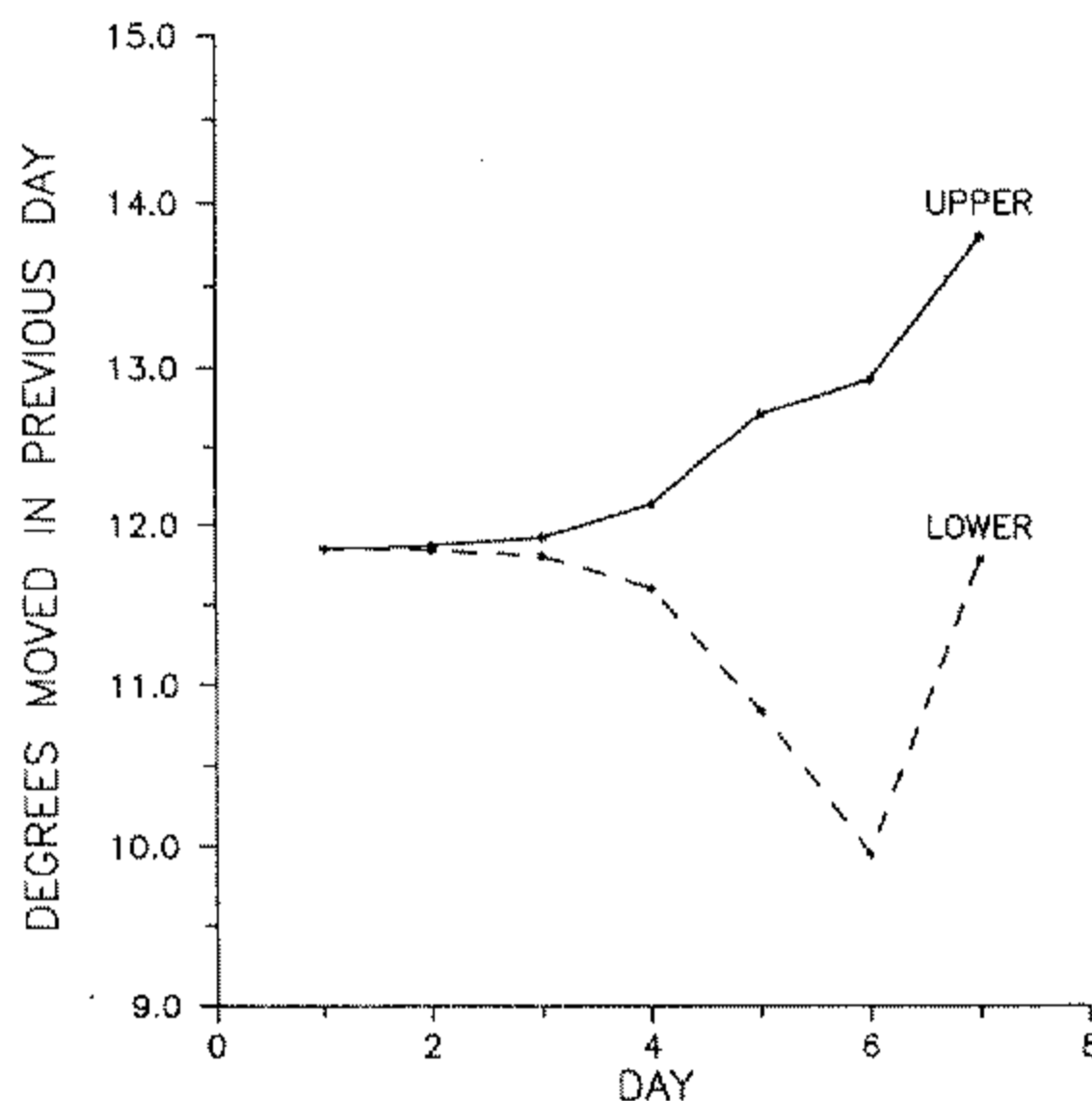


Figure B.1. Distance moved in degrees by the  $\zeta_6^{11}$  vorticity coefficient in the previous day at  $\sigma = 0.287$  (upper) and  $\sigma = 0.967$  (lower). The notation means the spectral coefficient for zonal wavenumber 6 and total wavenumber 11.

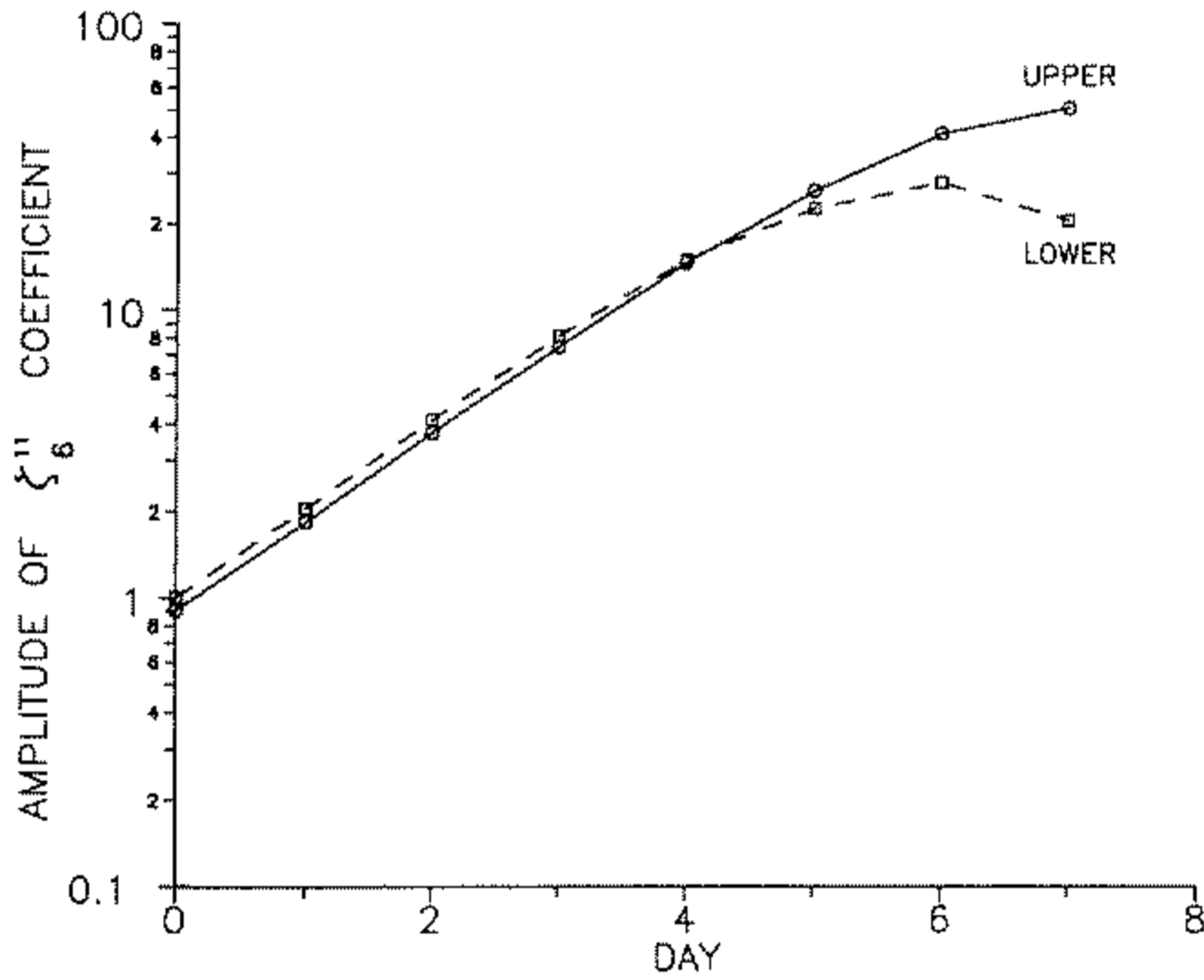


Figure B.2. Amplitude at the  $\zeta_6^{11}$  vorticity coefficient at  $\sigma = 0.287$  (upper) and  $\sigma = 0.967$  (lower) during the first 7 days. The notation means the spectral coefficient for zonal wavenumber 6 and total wavenumber 11;  $\zeta_6^{11}$  is measured in units of  $\Omega$  where  $\Omega$  is the earth's angular velocity. The scale is logarithmic.

At day 5,  $c$  varies by about  $\pm 1$  degree longitude per day. The relative acceleration of the upper wave is consistent with the observation noted in SH and TH that the system becomes more nearly equivalent-barotropic. This does not greatly affect the broad-scale features of  $K$  discussed above, although, for what it is worth, we note that the slight increase in  $c$  in the upper troposphere at day 5 will marginally increase  $K$  values there.

#### REFERENCES

- |                                                     |      |                                                                                                                                                                      |
|-----------------------------------------------------|------|----------------------------------------------------------------------------------------------------------------------------------------------------------------------|
| Andrews, D. G., Holton, J. R. and Leovy, C. B.      | 1987 | <i>Middle atmosphere dynamics</i> . Academic Press. San Diego, California                                                                                            |
| Andrews, D. G. and McIntyre, M. E.                  | 1978 | On wave action and its relatives. <i>J. Fluid. Mech.</i> , <b>89</b> , 647–664                                                                                       |
| Batchelor, G. K.                                    | 1967 | <i>An introduction to fluid dynamics</i> . Cambridge Univ. Press                                                                                                     |
| Berrisford, P.                                      | 1988 | 'Potential vorticity in extratropical cyclones'. PhD Thesis, Reading University                                                                                      |
| Carlson, T. N.                                      | 1980 | Air flow through mid-latitude cyclones and the comma cloud pattern. <i>Mon. Weather. Rev.</i> , <b>108</b> , 1498–1509                                               |
| Charney, J. G.                                      | 1948 | On the scale of atmospheric motions. <i>Geophys. Publ.</i> , <b>17</b> (2), 3–17                                                                                     |
| Charney, J. G. and Drazin, P. G.                    | 1961 | Propagation of planetary-scale disturbances from the lower into the upper atmosphere. <i>J. Geophys. Res.</i> , <b>66</b> , 83–109                                   |
| Clough, S. A., Grahame, N. S. and O'Neill, A.       | 1985 | Potential vorticity in the stratosphere derived using data from satellites. <i>Q.J.R. Meteorol. Soc.</i> , <b>111</b> , 335–358                                      |
| Danielsen, E. F.                                    | 1964 | Project Springfield Report, DASA 1517. Defense Atomic Support Agency, Washington DC                                                                                  |
|                                                     | 1980 | Stratospheric source for unexpectedly large values of ozone measured over the Pacific Ocean during Gametag, August 1977. <i>J. Geophys. Res.</i> <b>85</b> , 401–412 |
| Davies, H. C., Schär, C. and Wernli, H.             | 1991 | The palette of fronts and cyclones within a baroclinic wave development. <i>J. Atmos. Sci.</i> , <b>48</b> , 1666–1689                                               |
| Dunkerton, T. J., Hsu, C. P. F. and McIntyre, M. E. | 1981 | Some Eulerian and Lagrangian diagnostics for a model stratospheric warming. <i>J. Atmos. Sci.</i> , <b>38</b> , 819–843                                              |
| Edmon, H. J., Hoskins, B. J. and McIntyre, M. E.    | 1980 | Eliassen-Palm cross-sections for the troposphere. <i>J. Atmos. Sci.</i> , <b>37</b> , 2600–2616 (see also corrigendum. <b>38</b> , 1115 especially second-last item) |
| Gill, A.                                            | 1982 | <i>Atmosphere and ocean dynamics</i> . Academic Press, London                                                                                                        |

- Golding, B. W. 1984 A study of the structure of mid-latitude depressions in a numerical model using trajectory techniques I: Development of ideal baroclinic waves in dry and moist atmospheres. *Q.J.R. Meteorol. Soc.*, **110**, 847–879
- Green, J. S. A. 1970 Transfer properties of the large-scale eddies and the general circulation of the atmosphere. *Q.J.R. Meteorol. Soc.*, **96**, 157–185
- Green, J. S. A., Ludlam, F. H. and McIlveen, J. F. R. 1966 Isentropic relative-flow analysis and the parcel theory *Q.J.R. Meteorol. Soc.*, **92**, 210–219
- Haynes, P. H. 1988 Forced, dissipative generalizations of finite-amplitude wave-activity conservation relations for zonal and nonzonal basic flows. *J. Atmos. Sci.*, **45**, 2352–2362
- 1989 The effect of barotropic instability on the nonlinear evolution of a Rossby wave critical layer. *J. Fluid Mech.*, **207**, 231–266
- Heckley, W. A. and Hoskins, B. J. 1982 Baroclinic waves and frontogenesis in a non-uniform potential vorticity semi-geostrophic model. *J. Atmos. Sci.* **39**, 1999–2016
- Held, I. M. and Hoskins, B. J. 1985 Large-scale eddies and the general circulation of the troposphere. *Adv. Geophys.* **28A**, 3–31
- Held, I. M. and Phillips, P. J. 1987 Linear and nonlinear barotropic decay on the sphere. *J. Atmos. Sci.*, **44**, 200–207
- Hines, K. M. and Mechoso, C. R. 1991 Frontogenesis processes in the middle and upper troposphere. *Mon. Weather. Rev.*, **119**, 1225–1241
- Hoskins B. J. 1980 Representation of the earth's topography using spherical harmonics. *Mon. Weather. Rev.*, **108**, 111–115
- 1983 'Modelling of the transient eddies and their feedback on the mean flow'. In *Large-scale dynamical processes in the atmosphere*. Eds. B. J. Hoskins and R. P. Pearce. Academic Press, New York
- 1990 'Dynamics of mid-latitude cyclones'. In *Extratropical Cyclones. Palmén Memorial Volume*. Eds. C. Newton and E. Holopainen. American Meteorological Society
- Hoskins, B. J. and Berrisford, P. 1988 The storm of 15–16 October 1987: A potential vorticity perspective. *Weather*, **43**(3), 122–129
- Hoskins, B. J. and Sardesamukh, P. D. 1987 Transient eddies and the seasonal mean rotational flow. *J. Atmos. Sci.* **44**, 328–338
- Hoskins, B. J. and Simmons, A. J. 1975 A multilayer spectral model and the semi-implicit method. *Q.J.R. Meteorol. Soc.*, **101**, 637–655
- Hoskins, B. J. and West, N. V. 1979 Baroclinic waves and frontogenesis. Part II: Uniform potential vorticity jet flows—cold and warm fronts. *J. Atmos. Sci.*, **36**, 1663–1680
- Hoskins, B. J., McIntyre, M. E. and Robertson, A. W. 1985 On the use and significance of isentropic potential vorticity maps. *Q.J.R. Meteorol. Soc.*, **111**, 877–946; also comments, **113**, 402–404
- Illari, L. and Marshall, J. C. 1983 On the interpretation of eddy fluxes during a blocking episode. *J. Atmos. Sci.*, **40**, 2232–2242
- James, I. N. 1987 Suppression of baroclinic instability in horizontally sheared flows. *J. Atmos. Sci.*, **44**, 3710–3720
- Juckes, M. N. and McIntyre, M. E. 1987 A high resolution, one-layer model of breaking planetary waves in the stratosphere. *Nature*, **328**, 590–596
- Karoly, D. J. and Hoskins, B. J. 1982 Three-dimensional propagation of planetary waves. *J. Meteorol. Soc. Jpn.*, **60**, 109–122
- Killworth, P. D. and McIntyre, M. E. 1985 Do Rossby-wave critical layers absorb, reflect or over-reflect? *J. Fluid Mech.*, **161**, 449–492
- Marcus, P. S. 1990 Vortex dynamics in a shearing zonal flow. *J. Fluid. Mech.*, **215**, 393–430
- Matsuno, T. 1970 Vertical propagation of stationary planetary waves in the winter northern hemisphere. *J. Atmos. Sci.*, **27**, 871–883
- McIntyre, M. E. 1970 On the non-separable baroclinic parallel-flow instability problem. *J. Fluid. Mech.*, **40**, 273–306
- McIntyre, M. E. and Palmer, T. N. 1984 The 'surf zone' in the stratosphere. *J. Atmos. Terr. Phys.*, **46**, 825–849
- 1985 A note on the general concept of wave breaking for Rossby and gravity waves. *Pure Appl. Geophys.*, **123**, 964–975

- McIntyre, M. E. and Weissman, M. A. 1978 On radiating instabilities and resonant overreflection *J. Atmos. Sci.*, **35**, 1190–1196
- Randel, W. J. and Held, I. M. 1991 Phase speed spectra of transient eddy fluxes and critical layer absorption. *J. Atmos. Sci.*, **48**, 688–697
- Reed, R. J. and Albright, M. D. 1986 A case study of explosive cyclogenesis in the eastern Pacific. *Mon. Weather Rev.*, **114**, 2297–2319
- Rossby, C. G. 1936 Dynamics of steady ocean currents in the light of experimental fluid mechanics. Pap. Phys. Oceanogr. Meteorol. **5**(1), Mass. Inst. Tech. and Woods Hole Oceanogr. Inst., Eq. (75)
- Rhines, P. B. and Young, W. R. 1983 How rapidly is a passive scalar homogenized within closed streamlines? *J. Fluid Mech.*, **133**, 133–145
- Shapiro, M. A. and Keyser D. 1990 Fronts, jet streams and the tropopause. In *Extratropical Cyclones*, Palmén Memorial Volume. Eds. C. Newton and E. Holopainen. American Meteorological Society
- Shercliff, J. A. 1977 Simple rotational flows. *J. Fluid Mech.*, **82**, 687–703
- Shutts, G. J. 1986 A case study of eddy forcing during an Atlantic blocking episode. *Adv. Geophys.*, **29**, 135–162
- Simmons, A. J. 1974 The meridional scale of baroclinic waves. *J. Atmos. Sci.*, **31**, 1515–1525
- Simmons, A. J. and Hoskins, B. J. 1980 Barotropic influences on the growth and decay of nonlinear baroclinic waves. *J. Atmos. Sci.*, **37**, 1679–1684
- Stuart, J. T. 1967 On finite amplitude oscillations in laminar mixing layers. *J. Fluid Mech.*, **29**, 417–440
- Thomson, W. (Lord Kelvin) 1887 Stability of fluid motion—rectilinear motion of viscous fluid between two parallel planes. *Phil. Mag.*, **24**, 188–196
- Thorncroft, C. D. and Hoskins, B. J. 1990 Frontal cyclogenesis. *J. Atmos. Sci.*, **47**, 2317–2336
- Young, M. V., Monk, G. A. and Browning, K. A. 1987 Interpretation of satellite imagery of a rapidly deepening cyclone. *Q.J.R. Meteorol. Soc.*, **113**, 1089–1115